Photochemical & Photobiological Sciences (2024) 23:2133–2155
https://doi.org/10.1007/s43630-024-00648-w

ORIGINAL PAPERS

Similarity between oxygen evolution in photosystem II and oxygen reduction in cytochrome *c* oxidase via proton coupled electron transfers. A unified view of the oxygenic life from four electron oxidation–reduction reactions

Kizashi Yamaguchi[1,2,3] · Koichi Miyagawa[2] · Mitsuo Shoji[4] · Hiroshi Isobe[5] · Takashi Kawakami[3,6]

Received: 26 June 2024 / Accepted: 1 October 2024 / Published online: 22 November 2024

Abstract

Basic concepts and theoretical foundations of broken symmetry (BS) and post BS methods for strongly correlated electron systems (SCES) such as electron-transfer (ET) diradical, multi-center polyradicals with spin frustration are described systematically to elucidate structures, bonding and reactivity of the high-valent transition metal oxo bonds in metalloenzymes: photosystem II (PSII) and cytochrome *c* oxidase (C*c*O). BS hybrid DFT (HDFT) and DLPNO coupled-cluster (CC) SD(T_0) computations are performed to elucidate electronic and spin states of $CaMn_4O_x$ cluster in the key step for oxygen evolution, namely S_4 [S_3 with Mn(IV) = O + Tyr161-O radical] state of PSII and P_M [Fe(IV) = O + HO-Cu(II) + Tyr161-O radical] step for oxygen reduction in C*c*O. The cycle of water oxidation catalyzed by the $CaMn_4O_x$ cluster in PSII and the cycle of oxygen reduction catalyzed by the Cu_A-Fe_a-Fe_{a3}-Cu_B cluster in C*c*O are examined on the theoretical grounds, elucidating similar concerted and/or stepwise proton transfer coupled electron transfer (PT-ET) processes for the four-electron oxidation in PSII and four-electron reduction in C*c*O. Interplay between theory and experiments have revealed that three electrons in the metal sites and one electron in tyrosine radical site are characteristic for PT-ET in these biological redox reaction systems, indicating no necessity of harmful Mn(V) = O and Fe(V) = O bonds with strong oxyl-radical character. Implications of the computational results are discussed in relation to design of artificial systems consisted of earth abundant transition metals for water oxidation.

Graphical abstract

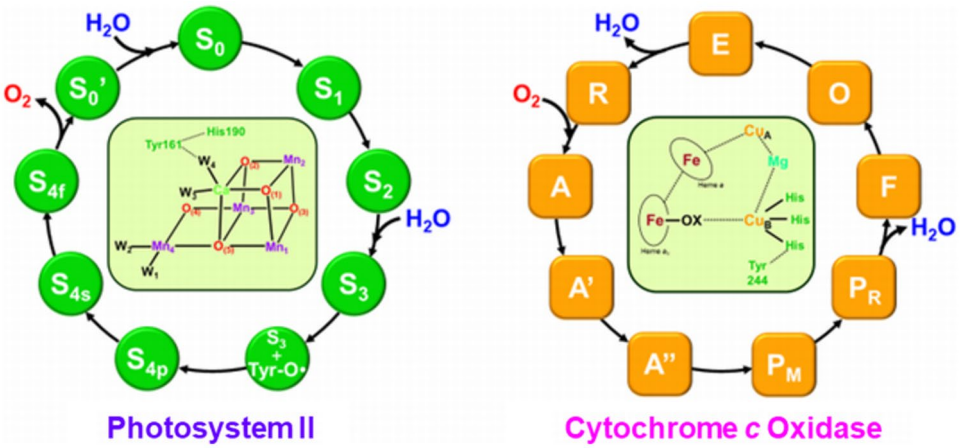

Keywords Broken symmetry · Photosystem II · Cytochrome *c* oxidase · Proton transfer coupled electron transfer · Strongly correlated electron systems

Extended author information available on the last page of the article

1 Introduction

Oxygen evolution reaction (OER) and oxygen reduction reaction (ORR) are fundamental processes in chemical and biological systems. Water oxidation in photosystem II (PSII) [1, 2] is one of OERs, which is a first step for biological photon to chemical energy conversion for oxygenic life on the earth. PSII for water oxidation is a large protein complex embedded in the thylakoid membranes of cyanobacteria, algae, and plants, and is the only known biological system that has the unique capability of utilizing visible light for the oxidation of water molecule into molecular oxygen as shown in Eq. (1) [1, 2]. However, direct water oxidation is not feasible by visible light. Therefore, the conversion of the light energy into chemical energy is catalyzed with the $CaMn_4O_x$ cluster in oxygen evolving complex (OEC) of PSII as follows.

$$2H_2O + 4h\nu + \left(CaMn_4O_x\right) \rightarrow O_2 + 4e^- + 4H^+_{lumen} + \left(CaMn_4O_x\right) \quad (1)$$

Electrons and protons generated by this reaction are transported by the aid of plastoquinone (PQ) within the thylakoid membrane in PSII. The Eq. (1) is often re-written by using PQ and protons in the stroma and lumen.

$$2H_2O + 2PQ + 4H^+_{stroma} \rightarrow O_2 + 2PQH_2 + 4H^+_{lumen} \quad (2)$$

Therefore, PSII is often referred to as a water-plastoquinone oxidoreductase in photosynthesis [1, 2]. Molecular oxygen (O_2) is a high-energy compound produced by water oxidation, which is essential for sustaining the oxygenic life via respiration and for the formation of ozone layer, which protects life from UV radiation damage on the earth [1].

The electrons and protons generated in Eq. (1) are transferred through a series of protein complexes in the cytochrome (Cyt) b_6f and photosystem I (PSI), and they are finally used for the reduction of $NADP^+$ into NADPH in Eq. (3) and for formation of adenosine triphosphate (ATP) from adenosine diphosphate (ADP) and phosphate (P_i) in the photo-phosphorylation in Eq. (4) [1, 2]:

$$2NADP^+ + 4e^- + 2H^+_{stroma} \rightarrow 2NADPH \quad (3)$$

$$3ADP + 3P_i + 6H^+_{lumen} \rightarrow 3ATP + 6H^+_{stroma} \quad (4)$$

NADPH and ATP provide the reducing power and energy for the reduction of CO_2 into carbohydrates in the dark reaction of the native photosynthesis [1, 2]. Conversion reaction of CO_2 into carbohydrates is referred to as the Calvin-Benson-Bassham (CBB) cycle [1] in the photosynthesis as

$$6CO_2 + 12NADPH + 18ATP \rightarrow 6C_6H_{12}O_6 + 12NADP^+ + 18ADP + 18P_i \quad (5a)$$

where 6 ATP molecules are used for the recycle of this CO_2 fixation process. Thus, total photon energies obtained by the series (Z)-scheme of the PSI and PSII are converted into chemical energy of carbohydrates through the CBB cycle in the photosynthesis.

Cellular respiration [1, 3, 4] is regarded as the reverse process in the oxygenic photosynthesis. Carbohydrate formed in Eq. (5a) is transformed into chemical energy of ATP for oxygenic life on the earth through the oxidative phosphorylation as follows.

$$C_6H_{12}O_6 + 6O_2 + 38ADP + 38P_i \rightarrow 6CO_2 + 6H_2O + 38ATP \quad (5b)$$

where 38 is the maximum number for generation of ATP molecules in glycolysis. The key steps involved in the respiration are the oxygen reduction reaction (ORR) and the proton pump catalyzed by the complex IV of mitochondria, cytochrome *c* oxidase (C*c*O) [3, 4]. The molecular oxygen reduction into water molecules by four electrons in the C*c*O of the respiratory system (mitochondria) is just regarded as the reverse reaction in Eq. (1). According to Wikström [3], the O–O bond energy obtained from four photons in Eq. (1) is used as driving force for transfer of four protons from N-side (higher *p*H compartment) to P-side (lower *p*H compartment) for ATP formation as shown in Eq. (6).

$$4Fe(II)(Cyt\ c) + 8H^+_{lumen(P)} + O_2 + (CcO) \rightarrow 2H_2O + 4H^+_{stroma(N)} + 4Fe(III)(Cyt\ c) + (CcO) \quad (6)$$

C*c*O is consisted of the four sites (Cu_A (Cu_2S_2), $heme_a$, $heme_{a3}$, Cu_B) and Mg^{2+}, which are responding to the catalytic site (Mn_2, Mn_3, Mn_4, Mn_1, and Ca) for water oxidation in OEC of PSII as illustrated in Fig. 1, where these active sites are embedded in protein matrices. Mechanistic similarities are expected between oxygen evolution in OEC and oxygen reduction in C*c*O from events of concerted or stepwise proton and electron transfers in Eqs. (1)–(6), although the structural constructions are different between them as shown in Fig. 1. Tri-copper cluster (MCO) in Fig. 1c [5, 6] also undergoes four-electron reduction of molecular oxygen into water molecule coupled with mono-oxygenation of substrates such as methane. Solomon et al. [5, 6] have pointed out the similarity between C*c*O (Cu_A (Cu_2S_2), $heme_a$, $heme_{a3}$, Cu_B) and MCO (T1-Cu, T2-Cu, Cu T3 pair). Thus, the metal-clusters play crucial catalytic roles for redox processes, indicating the necessity of theoretical models and computational procedures for treating one-electron processes coupled with proton transfer (see supplementary section SVI).

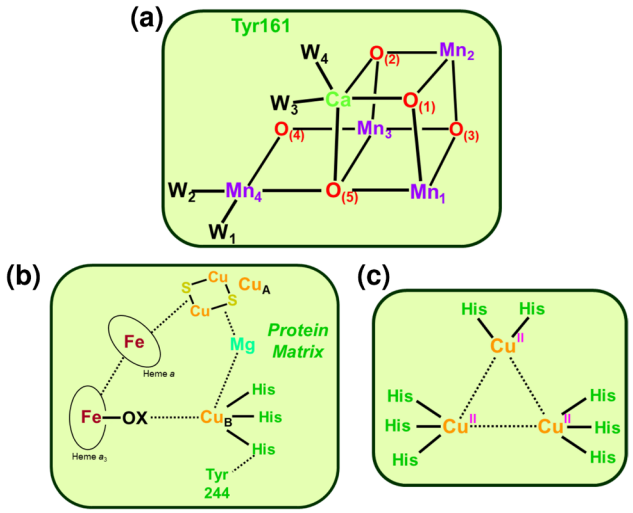

Fig. 1 Schematic illustrations of multi-nuclear cluster catalysts for **a** photosystem II (PSII) [1, 2], **b** cytochrome *c* oxidase [3, 4], and **c** multicopper oxidase (MCO) [5, 6]. PSII catalyzes water oxidation into molecular oxygen. The C*c*O catalyzes the four-electron reduction of molecular oxygen to water. The MCO with $Cu(II)_3$ similar to the Fe_2-Cu_B site of C*c*O (with T1) can catalyze methane oxidation

Three dimensional (3D) structures of the above metalloenzymes are crucial for elucidation and understanding of their biological functions. X-ray diffraction (XRD) analysis of PSII from *Synechococcus elongatus* was initiated in 2001 [7]. High-resolution (HR) XRD structures of the $CaMn_4O_x$ cluster in PSII [8] and formal $MgCu_2Fe_2$ cluster in C*c*O [9] have been elucidated, providing structural foundations for investigation of the catalytic cycles of four electron oxidation–reduction processes. The exchange-coupled site of Mn_4-X-Mn_1 site in $CaMn_4O_x$ catalyzes the oxidation of two water molecules (X = (H_2O OH_2) into molecular oxygen (X = [O = O]). On the other hand, the exchange-coupled sites of Fe_{a3}-X-Cu_B in C*c*O and T3 pair in MCO are regarded as the reduction site of molecular oxygen (X = [O = O]) into two water molecules (X = (H_2O OH_2). The thermodynamics of the conversion of water molecules to molecular oxygen in aqueous solution (*p*H = 7) requires four photons ($4h\nu$) as the energy source for the oxidation reaction as shown in Eq. (1) [1, 2]. On the other hand, the reverse downhill potential for oxygen reduction to water molecules by C*c*O is used as the driving force for proton-pumping reactions for ATP synthesis as shown in Eq. (6) [3, 4, 10, 11]. Judging from Eqs. (1)–(6), electron transfer (ET), proton transfer (PT), and PT coupled ET (PT-ET) processes play important roles for the elementary steps in PSII and C*c*O. Theoretically, the broken-symmetry (BS) and post BS methods are applicable to redox reactions responding to one electron processes in chemistry and biology.

Hoganson et al. [12] and other groups [13–16] have pointed out the similarity between the four electron processes in PSII and C*c*O. They have proposed that both Tyr161-O radical in PSII and Tyr244-O radical in C*c*O play important roles for four successive electron transfers in water oxidation and oxygen reduction, respectively. However, these proposals have not been conclusive because of lack of reliable geometric information of the intermediates in PSII. Recently, SFX-XFEL experiments [17–19] have provided structural information of the intermediates in the catalytic reactions in the oxygen evolution in PSII and oxygen reduction in C*c*O, providing the structural foundations for theoretical investigations of the mechanisms of these reactions. Over past decades, we have performed BS HDFT and coupled cluster (CC) single, double (SD) with perturbative triple (T) computations based on the natural orbital (UNO) of HDFT as trials, elucidating the structure, bonding, and reactivity of the $CaMn_4O_x$ cluster in PSII. Recent extensive reviews [3, 4] have summarized significant information on the structure, bonding, and reactivity of C*c*O, elucidating possible intermediates structures for the oxygen reduction. Therefore, the accumulated information for water oxidation in PSII and oxygen reduction in C*c*O has provided a chance to obtain deep insight of front and back relationship in these four electron redox reactions.

In this paper, we first describe basic concepts and theoretical foundations of BS DFT [20–25] and CC methods [26–31] for strongly correlated electron systems (SCES) such as $CaMn_4O_x$ in PSII and Cu_A-Fe_a-Fe_{a3}-Cu_B in C*c*O, for which four degrees of freedom, spin, charge, orbital, and dynamical nuclear motion, play important roles for determination of their structure, bonding, and reactivity. The concept of instability in chemical bonds [20, 23–25] and resulting BS solutions followed by the post BS procedures such as configuration interaction (CI) and CC are applied to molecular orbital descriptions of homolytic diradicals [32], electron transfer (ET) diradicals [33], and complex radical systems such as triangle metal clusters with spin frustration [34, 35] in sections II. Analytic solutions of two-electron two-orbitals [2e, 2o] and three-electron three-orbitals [3e, 3o] based on the Hubbard model [36] and DFT computational results for Mn_3O_4 clusters are given to elucidate spin frustrations in the supplementary section (see SII).

The BS methods are extended to the PT-ET processes for examination of one electron transfer (OET) redox reaction in section III. BS computations are performed to elucidate characteristic changes of the $CaMn_4O_x$ cluster in the S_0–S_3 states of the Kok cycle [37] for water oxidation in section IV. BS computations based on a large-scale quantum–mechanical (QM) model for the catalytic site for water oxidation in PSII are performed for the early S_4 state, namely [S_3 plus tyrosine 161 radical] state in section V. Large-scale QM computations for the catalytic site of C*c*O are also performed to elucidate structure and bonding of the so-called key P_M intermediate in section VI. Similarity

of the oxidation–reduction processes in PSII and C*c*O are examined based on these theoretical results in section VII, indicating that total of three electrons in the metal clusters and one electron in tyrosine radical are indeed operative in both PSII and C*c*O although the environmental amino acid residues for them are different [20]. Implications of the present results are discussed in relation to design of artificial water oxidation and oxygen reduction systems in the concluding section VIII.

2 Basic concepts of broken symmetry (BS) and post BS methods for oxygenation reactions

2.1 Instability in chemical bonds and emergence of the oxyl-radical character for photocatalysis

Band models have been used for understanding and explanation of water oxidation in artificial photosynthesis. In this paper, broken symmetry (BS) real-space models are used for theoretical investigations of redox reactions. Fundamental concepts and physical foundations of the BS and post BS methods are described to elucidate scope and reliability of these methods for strongly correlated electron systems (SCES) (see details in the supplementary section SI) [38–51]. The HOMO–LUMO energy gap is important for BS model of chemical bond. For example, molecular oxygen (O = O) in Eq. (1) is in the triplet (↑O = O↑) ground state [32] because of the zero HOMO–LUMO energy gap and Hund rule. Water oxidation in Eq. (1) indicates the generation of triplet molecular oxygen from closed-shell $2H_2O$ via spin catalysis of the $CaMn_4O_x$ cluster, indicating spin concept for open-shell species.

Triplet instability condition for bifurcation of the closed-shell orbital into two open-shell orbitals is important for understanding of singlet diradical. We first proposed the HOMO–LUMO mixing procedure [32] to obtain the broken-symmetry (BS) orbitals, which are mainly localized on the left- and right-radical sites, respectively. Several chemical indices such as diradical character are derived for elucidation of structure and bonding of active oxygens and oxy-radicals in photochemical reactions. Some of chemical indices are commonly defined for BS and post BS methods as shown in SI.

BS theoretical models were applied to photocatalysis reactions discovered in 1970s–1980s [52–55]. The titanium-oxo bond was regarded as an ionic bond Ti(IV)-O^{2-} responsible for nucleophilic reactions [56, 57]. On the other hand, photoexcitation entails conversion from Ti(IV)-O^{2-} into ↑•Ti(III)-O^{1-}•↓ with the oxyl-radical character responsible for radical reactions [57]. Photo-induced oxyl-radical site, undergoes the oxygenation reactions, providing, for example, peroxide (HOOH) which is often converted into singlet diradical HO•↑…↓•OH described by BS model [57]. BS methods have been successfully used for theoretical investigations of radical reactions by active oxygen (atomic oxygen (•O•), singlet molecular oxygen (↑O = O↓)) [58] and oxyradicals (•OOH, •OH) generated in photocatalysis [52–58]. Here, BS methods [32, 57, 58] are extended to theoretical investigations of multi-center polyradicals generated in PSII and C*c*O.

2.2 Instability in metal-oxo bonds of the oxyl-radical character for radical coupling reaction

The oxyl-radical character of the high-valent (HV) transition-metal oxo bonds (M = O) is a key concept for understanding of radical reactions of these species [59–61]. In 1979, Groves et al. [59] discovered the oxyl-radical reactivity (•M–O•) of the HV M = O bonds, which is very important for understanding of rebound mechanism for mono-oxygenation and radical coupling (RC) mechanism for the O–O bond formation. In early 1980s, we have performed BS MO computations [62] to explain the radical reactivity [59] of the HV 3d M = O bonds for which the energy gap between the dπ-pπ bonding (HOMO) and dπ-pπ* antibonding (LUMO) orbitals is usually small in contrast to HV 4d (5d) transition metal-oxo species [62]. For example, the HOMO–LUMO energy gap given by $\Delta\varepsilon = \varepsilon_{LUMO} - \varepsilon_{HOMO}$ is zero for the iron-oxo bond Fe(IV) = O, indicating the triplet ground state, (↑Fe(IV) = O↑) [58, 62], which is generated in the P_M state of C*c*O [3, 4] under discussion (see later). Similarly, the HOMO–LUMO gap becomes often smaller than the on-site electron repulsion integral (*U*) in the case of HV 3d M = O bonds, indicating the triplet instability condition [23–25] which induces the HOMO–LUMO mixing [32] to give the BS orbitals mainly localized on the M and O site respectively as shown in Fig. 2 [62]. The nearly localized electron (spin) on the oxygen site [62] may be regarded as the singly occupied MO (SOMO)-electron responding to radical reactions such as radical coupling (RC) reaction [59].

Past decades, the oxyl-radical character of the HV 3d M = O bonds [62] have been a guiding principle for understanding and explanation of their chemical reaction pathways [59–61, 63]. This spin-polarized state is often expressed as •M–O• in chemistry, where • means a local spin. The RC mechanism for water oxidation is feasible for the oxyl-radical sites as shown in Eq. (7a). On the other hand, acid–base (AB) ionic mechanism is feasible for 4(5)d-metal oxo bonds in Eq. (7b).

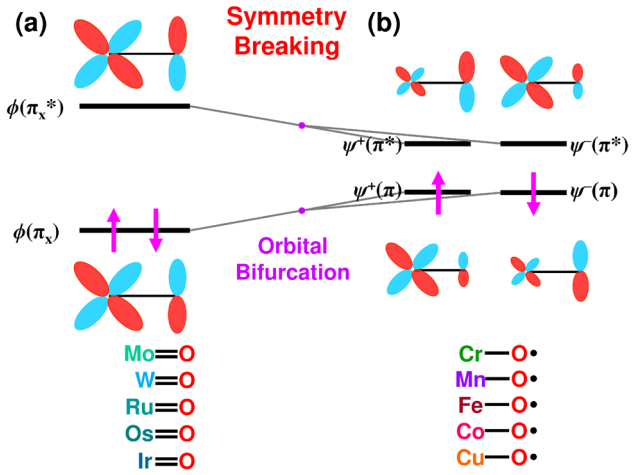

Fig. 2 **a** The closed shell metal-oxo bond M=O with the large HOMO–LUMO gap of 4d (5d) transition metals in the periodic table. **b** The HOMO–LUMO mixing occurs if the gap becomes smaller than the electron–electron repulsion term, entailing the broken-symmetry (BS) orbitals localized on the 3d transition metal (M) and O sites, respectively [62]. The localized orbital on the O site is responsible for the oxyl-radical reactivity [63]

$$\bullet\text{M-O}\bullet + \bullet\text{O-M}\bullet \rightarrow \bullet\text{M-O} - \text{O-M}\bullet \ (\text{M} = \text{Mn, Fe, Cu, } \ldots) \tag{7a}$$

$$\text{M} = \text{O} + \text{H}_2\text{O}\,(\text{OH}^-) + \text{B(base)} \rightarrow \text{M-OOH} + \text{BH}^+ (\text{M} = \text{Ru, Ir, } \ldots). \tag{7b}$$

Many experimental investigations have been performed for the above processes. From the theoretical site, careful examinations are crucial for evaluation of the oxyl-radical character in Eq. (7a).

Over past decades, hybrid DFT (HDFT) methods [64] consisted of the mixing of the exchange terms by the Kohn–Sham DFT and Hartree–Fock solutions have been employed for theoretical investigations. However, the oxyl-radical character [62, 63] is variable with the weight of the Hartree–Fock exchange term (w) in the HDFT models [64]. Therefore, the w-values have been assumed to be variable in the 10–20% range [65] in many papers. Relative energies among several intermediates in the S_i state for the Kok cycle for water oxidation are also variable with w [63, 66], indicating a semi-theoretical nature of HDFT for strongly correlated electron systems (SCES) such as $CaMn_4O_x$ in PSII [1, 2] and $MgCu_2Fe_2$ in C*c*O [3, 4]. Thus, beyond HDFT computations have been inevitable to examine scope and reliability of HDFT results for SCES [67]. To this end, coupled-cluster (CC) single, double (SD) and perturbation triple (T) excitation method [29, 30] using domain-based pair natural orbitals (DLPNO) [68, 69] is employed as a practical beyond DFT method. We have developed practical and efficient procedures for applications of time-consuming DLPNO-CCSD(T_0) methods to QM cluster models in the S_0–S_3 states of for OEC of PSII [70–72]. The comparison between HDFT and DLPNO-CCSD(T_0) results in turn has provided a reasonable w value for SCES under examinations [70–72]. In this paper, DLPNO-CCSD(T_0) computations based on an extended QM (283 atoms) model are performed for possible intermediates in the early S_4 state, namely [S_3 + Tyr-O radical] state to elucidate the mechanism of water oxidation in the Kok cycle of OEC of PSII.

2.3 Extension of BS models for multi-center systems with spin frustration

Recently, the multi-center transition-metal clusters in Fig. 1 have attracted great interest for four-electron redox reactions, indicating the revival of the spin frustration phenomena [73, 74]. Nocera group [75] have investigated the triangular and kagome clusters of the copper Cu(II) ions for water oxidation. Solomon group [5, 6] have investigated the $Cu(II)_3$ clusters for oxygen reduction in MCO as illustrated in Fig. 1c. Two antiferromagnetic (AF) and one ferromagnetic (F) spin pairs are formed in the low-spin collinear (up or down) spin model of the $Cu(II)_3$ cluster as illustrated in Fig. 3, providing three different spin alignments with the same energy: this is often referred to spin frustration. On the other hand, three F spin pairs are formed in the one high-spin (↑-↑-↑) configuration, whereas three AF spin pairs are feasible in the three non-collinear spin alignments as shown in Fig. 3. Thus, metal oxides with spin frustrations have been investigated in both material science [73, 74] and biological science [5, 6, 75]. Particularly, the geometric deformation from regular triangle or cubane structure with spin frustration into corresponding distorted structure via the Jahn–Teller (JT) effect of Cu(II) and Mn(III) ions is one of the key concepts for theoretical understanding of high reactivity of the distorted chair structure of the OEC of PSII. Early theoretical investigations [76, 77, 79–85] on the spin frustration systems [78] are given in the supplementary materials (SI).

The key concept for the spin frustration system is a quantum resonance among three collinear or noncollinear spin structures as illustrated in Fig. 3, providing resonating valence bond (RVB) [73] and resonating BS (RBS) [85] states. The collinear spin structures are expressed with the conventional UHF BS model. On the other hand, the noncollinear spin structures are given by general Hartree–Fock (GHF) solution with two component spinors, namely general spin orbitals (GSO) [80, 81]. From Fig. 3b, approximate spin projection (AP) GHF [67, 76, 85] provides the similar potential curve to that of Res GHF CI, indicating its reliability for theoretical investigation of spin-frustrated systems such as the triangular cluster in Fig. 1c. In fact, the $CaMn_3O_4$ cluster in the London model for PSII [83] was found to be a typical example of the spin frustration systems [84] (see

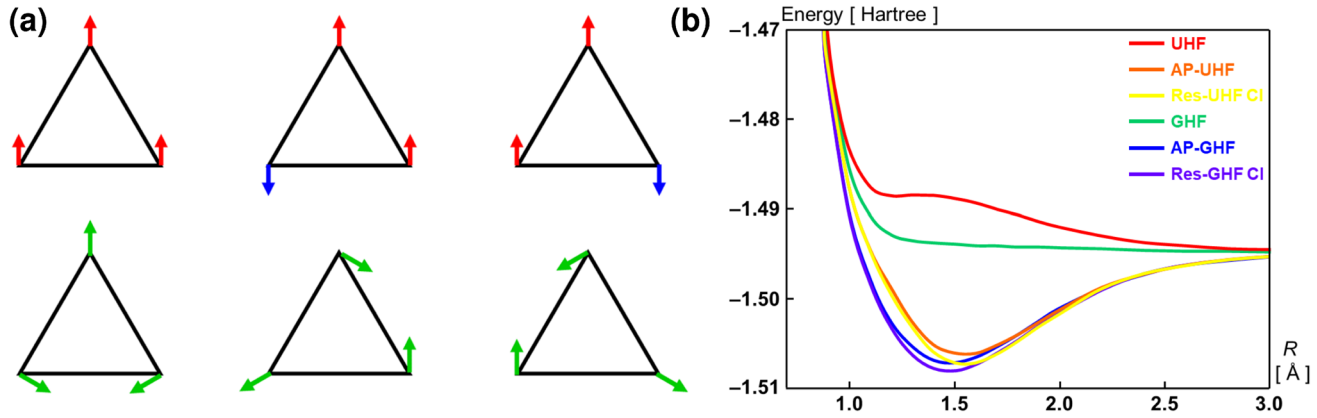

Fig. 3 **a** Collinear and non-collinear spin structures by axial (one dimensional) spin density wave (SDW) and helical (two dimensional) SDW (HSDW) solutions, where red and blue arrows indicate up (↑) and down (↓) spin, respectively by the collinear treatment and green arrows indicate the spin structures by the non-collinear treatment (see details in SI.10), **b** potential curves for the triangle H_3 radical with spin frustration by GHF, UHF, AP-UHF, AP-GHF, Res-UHF-CI, and Res-GHF-CI methods [74, 80, 82, 84, 85]

SI.9). On the other hand, the $CaMn_4O_5$ cluster discovered by Umena et al. [8] has exhibited a distorted chair structure without spin frustration [86, 87] via the JT effect of the Mn(III) ion with high chemical reactivity. The collinear spin model is here applied to elucidate structure and bonding of the $CaMn_4O_x$ cluster in the S_4 state.

2.4 Post BS computations by using the natural orbitals (UNO) of BS solutions

BS and post BS approaches to SCES starting from the stability analysis [31–35] are now handy and practical for investigation of metalloenzymes such as PSII, C*c*O, MCO, etc. However, dynamical correlations effect is crucial for examination of scope and applicability of the BS HDFT and RBS models for multi-nuclear systems in Fig. 1. To this end, UCCSD(T) and GCCSD(T) [30, 31] are necessary for inclusion of dynamical correlations within the single reference approximation as shown in Fig. 4. However, these computations are hardly possible for the $CaMn_4O_x$ cluster in OEC of PSII. An approximate version of the CC approach, DLPNO-CCSD(T_0), has been used for practical reasons in this paper. Resonating CC method are also desirable for spin frustration systems as shown in simple model systems [85]. The multi-reference (MR) CI [88–90] and CC using the natural orbital (UNO) of the BS solutions [31, 35, 90] have been proposed for inclusion of dynamical correlations as illustrated in Fig. 4. Recently, the Mukherjee-type MRCC computations [91, 92] have been performed for binuclear copper complexes to elucidate scope and applicability of the HDFT oxides. We expect similar successful results for UNO MR CC computations of the $CaMn_4O_x$ cluster. However, those are impossible at the moment in our computer system. Future UNO quantum computations (QC) [21, 93] are desirable for quantitative investigations of complexes systems with large UNO CAS space. In this paper, the interplay between DLPNO-CCSD(T_0) and spectroscopic results is employed as a feasible and practical procedure (see the supplementary materials in SI and SV).

3 Proton coupled electron transfer processes in PSII and CcO

3.1 Broken symmetry solutions for electron transfer reactions

In the preceding section II, BS and post BS methods have been applied for homolytic radical systems, for example in Eq. (7a). However, redox reactions involving one electron transfers (ET) [33] often take place in biological systems. In fact, SFX XFEL [19] and Fourier transform infrared (FTIR) experiments [95] have elucidated proton-transfer coupled electron transfer (PT-ET) processes in water oxidation in OEC of PSII and oxygen reduction in C*c*O. PT-ET processes have been investigated by the Marcus theory [94], Here, alternately, BS models [33, 62] for one ET processes are extended to PT-ET reactions in PSII and C*c*O. The energy gap between HOMO of electron donor (D) and LUMO of electron acceptor (A) embedded in protein matrix often becomes small, indicating formation of an electron transfer (ET) diradical [$D^+\bullet\ldots A^-\bullet$] [33] by thermal and/or photochemical excitation.

In this section, the BS model is newly extended to ET diradical reaction. To this end, the ET parameter is defined by the difference of the Coulomb integrals (α) of the D-A

pair in the case of the Hubbard [36] and Hartree–Fock models [62] (see SI.1) as

$$y = \left(\alpha_{\mathrm{D}} - \alpha_{\mathrm{A}}\right)/U \tag{8}$$

where difference between the ionization potential (I_{p}) of D and electron affinity (E_{a}) of A is also used for the numerator in Eq. (8). The ET (redox) parameter (y) becomes small than 1.0, indicating the instability condition which entails the orbital bifurcation for the up and down spins as follows:

$$\psi_i^+ = \cos\left(\theta_1 + \theta_2\right)\phi_{\mathrm{D}} + \sin\left(\theta_1 + \theta_2\right)\phi_{\mathrm{A}}^* \tag{9a}$$

$$\psi_i^- = \cos\left(\theta_1 - \theta_2\right)\phi_{\mathrm{D}} + \sin\left(\theta_1 - \theta_2\right)\phi_{\mathrm{A}}^* \tag{9b}$$

where ϕ_{D} and ϕ_{A} are the HOMO of donor (D) and LUMO of acceptor (A), respectively, and two θ_1 and θ_2 parameters become necessary to describe the orbital bifurcations in the ET reactions. From Eqs. (9a) and (9b), the BS solutions for ET processes are given by

$$\begin{aligned}\left|\psi_i^+\psi_i^-\right| &= \left|\left(\cos\left(\theta_1 + \theta_2\right)\phi_{\mathrm{D}} + \sin\left(\theta_1 + \theta_2\right)\phi_{\mathrm{A}}^*\right)\right. \\ &\quad \left.\sigma_\uparrow\left(\cos\left(\theta_1 - \theta_2\right)\phi_{\mathrm{D}} + \sin\left(\theta_1 - \theta_2\right)\phi_{\mathrm{A}}^*\right)\sigma_\downarrow\right| \\ &= \left[\cos^2\theta_1\cos^2\theta_2 - \sin^2\theta_1\sin^2\theta_2\right]{}^1\Phi_{\mathrm{G}} \\ &\quad + \left[\cos^2\theta_1\sin^2\theta_2 - \sin^2\theta_1\cos^2\theta_2\right]{}^1\Phi_{\mathrm{DET}} \\ &\quad + \sqrt{2}\cos\theta_2\sin\theta_2\,{}^1\Phi_{\mathrm{OET}} - \sqrt{2}\cos\theta_1\sin\theta_1\,{}^3\Phi_{\mathrm{OET}}\end{aligned} \tag{10}$$

where ${}^1\Phi_{\mathrm{G}}$, ${}^1\Phi_{\mathrm{DET}}$, ${}^1\Phi_{\mathrm{OET}}$, and ${}^3\Phi_{\mathrm{OET}}$ denote the ground closed-shell configuration; $\psi_i^+ = \psi_i^- = \phi_{\mathrm{D}}$; $\left|\phi_{\mathrm{D}}\sigma_\uparrow\phi_{\mathrm{D}}\sigma_\downarrow\right|$, the two ET closed-configuration $\left|\phi_{\mathrm{A}}^*\sigma_\uparrow\phi_{\mathrm{A}}^*\sigma_\downarrow\right|$, singlet and triplet one ET diradical configurations consisted of the linear combinations of the one ET configurations of $\left|\phi_{\mathrm{D}}\sigma_\uparrow\phi_{\mathrm{A}}^*\sigma_\downarrow\right|$ and $\left|\phi_{\mathrm{D}}\sigma_\downarrow\phi_{\mathrm{A}}^*\sigma_\uparrow\right|$, respectively.

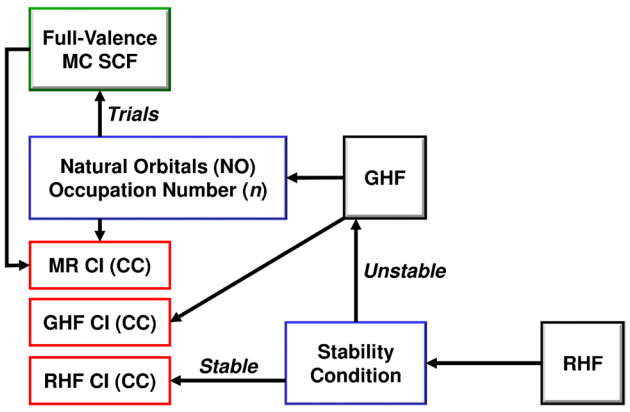

Fig. 4 Computational schemes for strongly correlated electron systems (SCES) [31, 35]. As a first step, broken symmetry (BS) computations are performed to elucidate the ground electronic and spin structures of SCES. Beyond BS calculations such as MR CI (CC) using the natural orbitals (UNO) or localized natural orbitals (ULO) of the BS solutions are performed for both ground and excited states of SCES. Scope and reliability of the BS computational results are examined by beyond BS computations

The ground state configuration with no ET diradical character is obtained by setting $\theta_1 = \theta_2 = 0$ which is responsible for the initial closed-shell state (DA); $\psi_i^+ = \psi_i^- = \phi_{\mathrm{D}}$; ${}^1\Phi_{\mathrm{G}} = \left|\phi_{\mathrm{D}}\sigma_\uparrow\phi_{\mathrm{D}}\sigma_\downarrow\right|$. On the other hand, the up and down spin orbitals are given by $\psi_i^+ = \phi_{\mathrm{A}}^*$ and $\psi_i^- = \phi_{\mathrm{D}}$ under the assumption of $\theta_1 = \theta_2 = \pi/4$, indicating the complete mixing state of singlet and triplet ET diradical configurations; ${}^1(\mathrm{D}^+\bullet\mathrm{A}^-\bullet)$ and ${}^3(\mathrm{D}^+\bullet\mathrm{A}^-\bullet)$.

$$\left|\psi_i^+\psi_i^-\right| = \frac{1}{\sqrt{2}}\left({}^1\Phi_{\mathrm{OET}} - {}^3\Phi_{\mathrm{OET}}\right), \left(\theta_1 = \theta_2 = \pi/4\right) \tag{11a}$$

$$\left|\psi_i^-\psi_i^+\right| = \frac{1}{\sqrt{2}}\left({}^1\Phi_{\mathrm{OET}} + {}^3\Phi_{\mathrm{OET}}\right), \left(\theta_1 = 3\pi/4 \text{ and } \theta_2 = \pi/4\right) \tag{11b}$$

The up and down spin orbitals are given by $\psi_i^+ = \phi_{\mathrm{A}}^*$ and $\psi_i^- = \phi_{\mathrm{A}}^*$ under the assumption of $\theta_1 = \pi$ and $\theta_2 = \pi/2$, indicating the two ET closed-configuration ${}^1\Phi_{\mathrm{DET}} = \left|\phi_{\mathrm{A}}^*\sigma_\uparrow\phi_{\mathrm{A}}^*\sigma_\downarrow\right|$. The wave-functions for the special configurations; $(\mathrm{D}^2\mathrm{A}^0) \rightarrow (\mathrm{D}^{+1}\bullet\mathrm{A}^{1-}) \rightarrow (\mathrm{D}^{++}\mathrm{A}^{2-})$ are easily obtained by Eqs. (9a) and (9b), suggesting the constructions of trial orbitals for BS computations for more general cases with variable covalent (x) and redox (y) parameters in biological systems [62]. Thus, BS models can describe both one and two electron transfer processes under the single Slater determinant approximation.

However, singlet BS solutions involve the triplet configuration as shown in Eqs. (10) and (11). Therefore, quantum resonance between them is necessary, providing the resonating BS (RBS) solutions, which are responsible for pure singlet and triplet ET diradical states as follows:

$$\begin{aligned}{}^1\Phi_{\mathrm{RBS}(+)} &= N\left\{\left[\cos^2\theta_1\cos^2\theta_2 - \sin^2\theta_1\sin^2\theta_2\right]{}^1\Phi_{\mathrm{G}}\right. \\ &\quad + \left[\cos^2\theta_1\sin^2\theta_2 - \sin^2\theta_1\cos^2\theta_2\right]{}^1\Phi_{\mathrm{DET}} \\ &\quad \left. + \sqrt{2}\cos\theta_2\sin\theta_2\,{}^1\Phi_{\mathrm{OET}}\right\}\end{aligned} \tag{12a}$$

$${}^3\Phi_{\mathrm{RBS}(-)} = N\sqrt{2}\cos\theta_1\sin\theta_1\,{}^3\Phi_{\mathrm{OET}} \tag{12b}$$

where N denotes the normalizing factor. The singlet RBS state given by ${}^1\Phi_{\mathrm{RBS}(+)}$ is similar to a partial ET state of the Mulliken's charge transfer (CT) theory [96]. On the other hand, the ${}^1\Phi_{\mathrm{RBS}(+)}$ state with large ET configuration is similar to the one ET state of Marcus ET theory [94]. The RBS model can trace variations of the weight of the one ET configuration along the ET reaction. In fact, the RBS states for the complete one ET structure in Eqs. (11a) and (11b) are given as

$$^{1}\Phi_{\mathrm{RBS}(+)} = \frac{1}{\sqrt{2}}\left(\left|\psi_i^{+}\psi_i^{-}\right| + \left|\psi_i^{-}\psi_i^{+}\right|\right) = {}^{1}\Phi_{\mathrm{OET}} \quad (13a)$$

$$^{3}\Phi_{\mathrm{RBS}(-)} = \frac{1}{\sqrt{2}}\left(\left|\psi_i^{+}\psi_i^{-}\right| - \left|\psi_i^{-}\psi_i^{+}\right|\right) = {}^{3}\Phi_{\mathrm{OET}} \quad (13b)$$

The energy gap between the singlet and triplet ET diradical state is given by $2J_{DA}$ because the Heisenberg model [20] is applicable in the region (see SIII).

The above BS models for one ET processes are effective to investigate the nature of the chemical bonds of the Fe-OO bond in C*c*O. Triplet molecular oxygen ($^3O=O$) is inserted into the Fe(II) site in the initial state (A) of the oxygen reduction in C*c*O, providing the triplet–triplet (T-T) exchange coupled total singlet configuration; $^1[^3Fe(II)\ldots {}^3O=O]$ (see Fig. 11). One ET reaction occurs at the next step (A'), giving the ET diradical configuration involving superoxide anion radical; $^1[^2Fe(III)\ldots {}^2O=O^-]$. Formation of the oxygen dianion is feasible in C*c*O by one ET from Cu(I) to the cluster; $^1[^2Fe(III)\text{-}^1O\text{-}O^{2-}\text{-}^2Cu(II)]$, which is the singlet diradical consisted of doublet Fe(III) and Cu(II) ions via the super-exchange coupling through oxygen dianion. Thus, BS model developed here is applied for theoretical modeling of the early redox reactions in C*c*O (see later).

3.2 Proton transfer coupled electron transfer reactions

The above BS ET model is extended to PT-ET process involving proton transfer to afford OOH bond in oxygen reduction in C*c*O. Proton-coupled redox reaction is a classic concept [97–101]. The proton- transfer (PT) process in biology is formally regarded as an ionic process as shown in Eq. (14a), where $D=M(X)\text{-}OH_2$ and $A=[O=M(Y)]$. On the other hand, the one ET process is formally regarded as a valence variation process as shown in Eq. (14b). The one ET process in Eq. (14b) is traced with the BS MO model as shown in the preceding section III.1. The proton transfer after the one electron transfer is also feasible as illustrated in Eq. (14c). Therefore, several cases are conceivable for coupled processes of PT and ET; (1) ET before PT, (2) PT before ET, and (3) the concerted proton transfer (PT) coupled electron transfer (ET) process (PT-ET) as shown in Eq. (14d). Figure 5 illustrates the PT-ET processes for Mn-oxo bonds.

$$M(X)\text{-}OH_2 + O = M(Y) \rightarrow M(X)\text{-}OH + HO\text{-}M(Y) \quad (14a)$$

$$M(X)\text{-}OH_2 + O = M(Y) \rightarrow M(X+1)\text{-}OH_2 + O = M(Y-1) \quad (14b)$$

$$M(X+1)\text{-}OH_2 + O = M(Y-1) \rightarrow M(X+1)\text{-}OH + HO\text{-}M(Y-1) \quad (14c)$$

$$\begin{aligned} M(X)\text{-}OH_2 + O = M(Y) &\rightarrow M(X+\delta)\text{-}OH \\ \ldots H \ldots O &= M(Y-\delta) \\ &\rightarrow M(X+1)\text{-}OH + HO\text{-}M(Y-1) \end{aligned} \quad (14d)$$

Recent time-resolved (TR) SFX XFEL [17, 18] and FTIR [95] experiments have elucidated possible PT and ET processes in the water oxidation in OEC of PII. PT-ET models in Eq. (14) are applied to investigate possible roles of tyrosine radical in the oxygen evolution reaction of PSII and the oxygen reduction reaction of C*c*O [19] in Eq. (15) (see later)

$$^1[^3Fe(IV) = O \ldots HO\text{-}^2Cu(II) \ldots {}^2 \cdot O\text{-}Tyr161] \quad (15)$$

4 Applications of BS and post BS models to the $CaMn_4O_x$ cluster in OEC of PSII

4.1 Structures and bonding of the $CaMn_4O_5$ cluster in PSII by XRD, XFEL, and EPR

Basic concepts and BS computational methods in sections II and III are applied to elucidate structure and bonding of the $CaMn_4O_x$ cluster in PSII. To this end, 3D geometric structures of PSII by XRD and SFX XFEL are indispensable for construction of reliable structural models for theoretical investigations. However, the experimental structures often suffered non-negligible experimental uncertainty at available resolutions (1.9–2.1 Å) [8, 17, 18]. Therefore, theoretical computations are expected to refine the geometric structures of the $CaMn_4O_x$ cluster by XRD [8] and XFEL [17, 18], which are crucial for successive investigations of electronic and spin structures of the OEC of PSII [20]. Indeed, BS and post BS (CC) methods in combinations with spectroscopic methods are effective for elucidation of structure and bonding of the $CaMn_4O_x$ clusters in OEC of PSII [1].

The magnetism and chemical bond are guiding principle for investigation of 3d transition metal complexes [102–108]. The manganese ions in the $CaMn_4O_x$ clusters

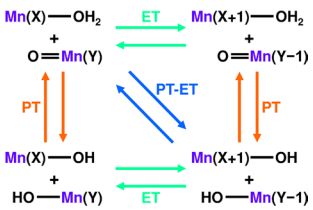

Fig. 5 Proton-transfer (PT) coupled one electron transfer (ET) reaction between the manganese oxo bond and manganese-water to provide manganese hydroxide bonds. Activation barrier for each process is highly dependent on reaction conditions

are assumed to be Mn(III) and/or Mn(IV) for OEC of PSII under the high-oxidation scenario based on the X-ray spectroscopy [109]. The manganese ions are found to be in the local high-spin states with weak ligand fields [104], Mn(III) with $S_a = 4/2$ and Mn(IV) with $S_b = 3/2$, embedded in the protein field of OEC. Judging from the spin populations by BS computations, the Heisenberg models [102] with the orbital-averaged effective exchange integrals (J_{ab}) [62, 106, 107] are also found to be applicable to investigate available magnetic properties of the $CaMn_4O_x$ clusters, which accord with the observed results by EPR [108] (see supplementary section SII).

In 2004, XRD experiment at the 3.5 Å XRD resolution [83] elucidated the triangular (non-collinear) spin state of the London model. However, the regular cubane structure [83] was relaxed into the distorted chair structure with the collinear spin state at the 1.9 Å XRD resolution [8] because of the JT effect of the Mn(III) ion. Therefore, eight spin structures were available for four site spin models under the axial (collinear) spin approximation [86], providing one total highest (HS) spin configuration, four total intermediates spin configurations and three total low-spin configurations as illustrated in Fig. S6(a) [86, 87]. Full geometry optimizations of these configurations revealed the most stable configuration, for which the J_{ab} values were determined by using total energies of the BS solutions with different spin structures [86, 87]. The J_{ab} values obtained indicated good coincidence with the observed values by EPR [108]. Here, the interplay between BS theory and EPR is extended to investigations of possible intermediates in the S_4 state of the Kok cycle [37].

4.2 Charge and orbital degrees of freedom for the $CaMn_4O_5$ cluster in PSII

The valence states of the Mn ions are important for elucidation of the mechanism of water oxidation in PSII. Historically, the low- and high-oxidation scenario have been proposed for the valence structures of $CaMn_4O_x$ cluster, providing $Ca(II)Mn(III)_4O_5$ and $Ca(II)Mn(III)_2Mn(IV)_2O_5$, respectively, in the dark stable state in the Kok cycle. The latter high-oxidation scenario was accord with the experimental results by XAS, EXAFS, and others [109, 110]. Theoretically, six different valence structures are available for the latter scenario as shown in Fig. S6(b) [86]. Therefore, total 8×6 (=48) spin-valence configurations are feasible for the dark stable S_1 structure of $CaMn_4O_5$ cluster as illustrated in Fig. S6(c) [86]. Total energies of these configurations were effective to elucidate the ground valence structure in the S_1 state, which is compatible with the EXAFS results [110]. Interplay between BS theory and EXAFS was useful for elucidations of stable valence configurations in the S_2 and S_3 states [87, 111] (see supplementary material). BS computations further revealed subtle geometry changes of the $CaMn_4O_5$ cluster by the JT effects (orbital degree of freedom) of the Mn(III) ion. Here, the BS methods are applied to elucidate the spin-valence-orbital configurations of the S_4 intermediates in the Kok cycle.

4.3 Proton shift degrees of freedom for the $CaMn_4O_5$ cluster in PSII

Early XRD structures [7, 83, 112] at 3.0–3.8 Å resolution provided positions of Mn ions but no information of positions of oxygen atoms in OEC of PSII. In 2011, Umena et al. [8] have discovered the high-resolution (HR) XRD structure of $CaMn_4O_5$ cluster at 1.9 Å resolution, elucidating the "distorted-chair like" structure of the $CaMn_4O_5$ cluster and positions of oxygen atoms within the $CaMn_4O_5$ cluster and those of water molecules around the $CaMn_4O_5$ cluster. However, hydrogen atoms were invisible by HR XRD [8]. Therefore, full geometry optimizations of the OM models adding hydrogen atoms for OEC by HR XRD [8] were necessary to obtain the refined structure in the S_1 state [86, 87].

First of all, we have performed the HDFT computations for the $Ca(II)Mn(III)_2Mn(IV)_2O_5(H_2O)_4$ cluster with six amino acid residues with the negative charge and neutral histidine ligand (His332) [86, 87]. Therefore, total positive charge for the model of **1** is 16 ($=2+3\times2+4\times2$) and total negative charge is -16 ($=-2\times5+-1\times6$) in the S_1 state. Our model is often referred to as the 4H model for the S_1 state in contradiction to the 3H model [108]. The spin populations were about 4.0 for all the Mn ions under the assumption of the HR XRD structure [8], indicating the internal reduction of two Mn(IV) ions into two Mn(III) ions. The total negative spin densities were found to be about 2.0 [86, 87], indicating the partial charge transfer from the oxygen dianions to the two Mn(IV) sites because of the elongated Mn(IV)-O^{2-} distances (the experimental uncertainty is about 0.16 Å for HR XRD [8]).

We have performed the full geometry optimization [86, 87] of the cluster to refine the geometrical parameters revealed by HR XRD [8]. The spin populations for the optimized geometry were about 4.0, 3.0, 3.0, and 4.0 for Mn_1, Mn_2, Mn_3, and Mn_4, respectively, indicating the Ca(II) $Mn(III)_2$ $Mn(IV)_2O_5$ $(H_2O)_4$ valence state which accord with the high-oxidation scenario for the $CaMn_4O_5$ cluster. This valence state is usually abbreviated as (3443) responding to the valence states of the Mn ions. The optimized Mn–Mn, Mn–O distances were also consistent with the EXAFS results [109, 110]. The full geometry optimizations by BS HDFT [87] were useful for elucidating the refined HR XRD structure, which was later found to be consistent with the damage free structure by the serial femtosecond crystallography (SFX) using the X-ray free electron laser (XFEL) [114]. The full geometry optimizations also elucidated

positions of H atoms and H–O distances for the parent S_1 structure, for which the HR XRD [8] and SFX XFEL [114] provided no information.

Protonation state of the oxygen dianions in the $CaMn_4O_5$ cluster is a moot point in the XRD structure [8]. We further performed full geometry optimizations of several proton-shifted geometrical isomers with the (3443) parent valence state from the coordinated water molecule (W2 or W1) to the oxygen dianion sites such as $O_{(5)}$ or $O_{(4)}$ sites [87]. To this end, the sites of the $CaMn_4O_5$ cluster were denoted as X (= $O_{(5)}$), Y (= W2), Z (= W1), U (= $O_{(4)}$), and W (= $O_{(6)}$) as shown in Fig. 6 [87]. The oxidation states of water molecules are also denoted as O^{2-} (= a), OH^- (= b), and H_2O (= c). According to the above notations, the parent S_1 structure is denoted as S_{1acca} where X = U = O^{2-} and W2 = W1 = H_2O and no water insertion of W in the S_1 state [87]. The proton-shifted S_1 structures are similarly expressed as S_{1abcb} where X = O^{2-}, Y = U = OH^-, and W2 = H_2O, and S_{1bbca} where U = O^{2-}, X = Y = OH^-, and W2 = H_2O. The hydrogen atoms are invisible by HR XRD [8] and SFX XFEL [114] at about 1.9–2.0 Å resolution, indicating no experimental information for discrimination among the S_1 isomers. Future high-resolution cryo-EM experiments are expected to provide reliable information to examine geometrical parameters for the proton-shifted isomers S_{1bbca} and/or S_{1abcb}.

4.4 Theoretical predictions of possible structures in the S_0, S_2, and S_3 states

Water oxidations in OEC of PSII proceed through five steps S_i (i = 0–4) in the Kok cycle [37] (see Fig. Fig. S8). The S_1 structure observed by HR XRD [8] corresponds to the dark stable state for the catalytic cycle of water oxidation. The refined distorted chair S_1 structure by full geometry optimization [87] in Fig. S9 was found to be reasonable as compared with available geometric parameters by the EXAFS [109]. Judging from the reasonable S_1 structure [87], the full geometry optimizations by HDFT were considered to be reliable for theoretical predictions of possible geometric structures in the S_i (i = 0, 2, 3) states of OEC of PSII. We indeed performed full geometry optimizations of possible geometric structures in the S_i (i = 0–3) states of the Kok cycle just after the discovery of the HR XRD structure [8] (see supplementary results in Fig. S7) [87].

Early predicted S_0, S_1, S_2, and S_3 structures in Fig. S7 [21, 70–72, 87] were found to be compatible with recent SFX XFEL results [116–119], indicating that full geometry optimizations by HDFT are reliable enough for searching reasonable geometries of possible intermediates in the Kok cycle. Refinements of the early geometric structures [87] by HDFT have been performed assuming several extended QM models [70–72] and QM/MM models [113, 115]. The computational results are now consistent with the observed results for the S_1, S_2 and S_3 states by the SFX XFEL experiments [17–19, 116–118]. Thus, BS (HDFT) [87] and DLPNO-CCSD(T_0) [70–72] methods are reliable for theoretical investigations of the redox reactions involving one electron transfer (ET) and proton transfer (PT) in the Kok cycle for water oxidation. After whole examinations of possible intermediates in the S_1, S_2, and S_3 states, full geometry optimizations by HDFT are reliable for investigations of possible geometric structures. On the other hand, DLPNO-CCSD(T_0) computations are essential for elucidation of relative energies between them. We can now perform HDFT and DLPNO-CC computations to elucidate the structure and bonding of possible intermediates in the final S_4 state.

5 Structure and bonding of the S_3 plus Tyr-O radical configuration

5.1 SFX XFEL results after the third flash

Recent SFX XFEL experiments [17, 18, 116–119] have elucidated that the one-electron transfer (OET) from Tyr161-OH to the cation radical of P680 takes place in the range of 50–100 μs after the third flash for the OEC of PSII, providing the cation radical of the Tyr161-OH which undergoes the proton transfer to N-site of His190 to form

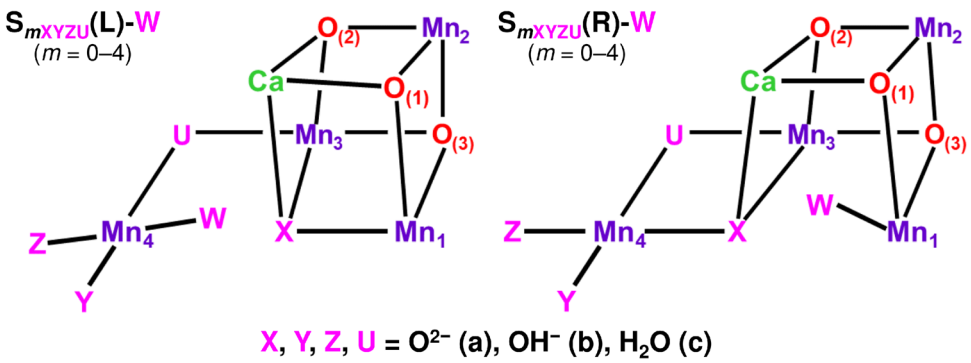

Fig. 6 The notations of the active sites of $CaMn_4O_x$ cluster in the Kok cycle for water oxidation in PSII are given as follows; X = $O_{(5)}$, Y = W2, Z = W1, U = $O_{(4)}$, and W = inserted water molecule (W_{INT}). The oxidation states of water molecules are denoted as a = O^{2-}, b = OH^-, and c = H_2O

the Tyr161-O• radical and H^+His190. Available experiments [1] have elucidated that the mutation of His190 with others entails the stop of water oxidation, implying the participation of His190 as a base (B) for proton acceptor. Therefore, the initial PT and ET process is regarded as the concerted PCET in Sect. 3.

According to the SFX XFEL results [116–118], the successive proton release from the [$CaMn_4$-Tyr161-O• core] to lumen occurs in the range of 250–500 μs before the one electron transfer from CaMn4-core to Tyr-161 radical; this ET process occurs in the long range of 500–1200 μs. Interestingly, the release of molecular oxygen was found to start after 1200 μs of the third flash [118]. This indicates an interesting possibility that the O–O bond formation in OEC of PSII is feasible without the one ET to Tyr161-O radical for formal formation of the Mn(V) = O site as in the case of no formation of Fe(V) = O in C*c*O [3–5] (see later). These experimental results have elucidated multistep reactions [95, 116–118] in the lag phase before the O–O bond formation, indicating the necessity of HDFT computations to elucidate possible structures in the early S_4 state for water oxidation.

5.2 Full geometry optimizations of the [S3 + Tyr-O•] based on an extended QM model

Recent SFX XFEL results [116–118] have suggested participation of tyrosine161 residue for the O–O bond formation. However, tyrosine161 was not included in our previous QM models (73, 103, 227 atoms) used for geometry optimizations of the S_1, S_2, and S_3 structures, indicating that the QM models were insufficient for structure determination of the early S_4 state; [S_3 + Tyr161-O• radical]. Therefore, a large QM (283 atoms) is newly constructed based on the previous QM models including key amino acid residues and water molecules as illustrated in Fig. 7. Full geometry optimizations of the [S_3 + Tyr-O•] intermediates based on the large QM model (283 atoms) are newly performed by UB3LYP-D2 method with def2-TZVP basis in the COSMO environment. Figure 8 illustrates the optimized geometries of the intermediate structures; (a) [S_{3abca}(R)-OH_{glu} + Tyr-O•], (b) [S_{3acca}(R)-Oxo + Tyr-O•], (c) [S_{3acca}(R)-Oxyl + Tyr-O•], and (d) [S_{3acca}(R)-Peroxide + Tyr-O•].

From Fig. 8a and d, the optimized Mn_1-Mn_2, Mn_2-Mn_3, Mn_3-Mn_4, Mn_1-Mn_3, and Mn_1-Mn_4 distances for [S_{3abca}(R)-OH_{glu} + Tyr-O•] are 2.79 (2.76), 2.86 (2.81), 2.75 (2.92), 3.57 (3.32), and 5.37 (5.19) Å, respectively, where the corresponding distances for [S_{3abca}(R)-Peroxide + Tyr-O•] are given in parentheses. The above Mn–Mn distances observed for the early S_4 state by SFX XFEL [118] are 2.77, 2.86, 2.75, 3.33, and 5.06 Å, respectively, which accord with

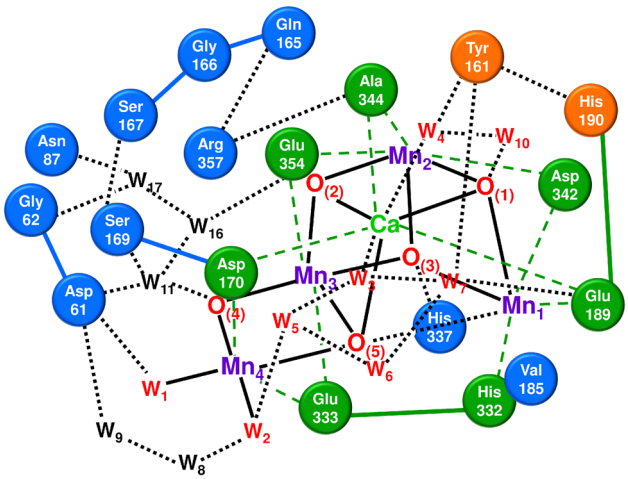

Fig. 7 An extended QM model (283 atoms) for geometry optimization by UB3LYP-D2 method. Tyr161 and His190 are newly included in the QM model to examine their participation of water oxidation in the S_4 state

those of the optimized values for by UB3LYP-D2 procedure, indicating the reliability of the geometry optimizations at the DFT plus dispersion (D2) level of theory. The Mn_3-Mn_4 distance is elongated by 0.17 Å after the $O_{(5)}$-$O_{(6)}$ bond formation, whereas the Mn_1-Mn_3 distance is shortened by 0.25 Å, indicating the characteristic geometric changes.

Before the peroxide formation, two different intermediates, [S_{3acca}(R)-Oxo + Tyr-O•] and [S_{3acca}(R)-Oxyl + Tyr-O•] are formed via proton transfer from $O_{(6)}H$ to W2 (= OH) as shown in Fig. 8c and d. The five Mn–Mn distances for the former (latter) intermediates are 2.80 (2.78), 2.83 (2.82), 2.75 (2.82), 3.49 (3.38), and 5.30 (5.24) Å. The Mn–Mn distances observed for A-monomer in the S_4 structure at 250 μs by SFX XFEL [118] are 2.86, 2.86, 2.75, 3.41, and 5.14 Å, respectively, which accord with those of the optimized values of the Mn-Oxo intermediate for by UB3LYP-D2.

The optimized Mn_1-$O_{(6)}$, Mn_4-$O_{(5)}$ and $O_{(5)}$-$O_{(6)}$ distances for [S_{3abca}(R)-OH_{glu} + Tyr-O•] are 1.81 (2.15), 1.81 (2.26), and 2.54 (1.42) Å, respectively, where the corresponding distances for [S_{3acca}(R)-Peroxide + Tyr-O•] are given in parentheses. The Mn_1-$O_{(6)}$ and Mn_4-$O_{(5)}$ distances for [S_{3abca}(R)-OH_{glu} + Tyr-O•] are about 1.8 Å, which accord with the Mn(IV)-O distance without the JT elongation. On the other hand, these distances for [S_{3acca}(R)-Peroxide + Tyr-O•] are about 2.2–2.3 Å, indicating the JT elongation of the Mn(III) ion. The $O_{(5)}$-$O_{(6)}$ distance is shortened by 1.12 Å with the $O_{(5)}$-$O_{(6)}$ bond formation. The resulted $O_{(5)}$-$O_{(6)}$ is compatible with that of peroxide (1.46 Å). Therefore, the valence states of the four Mn ions are (4444) and (3443) for the S_{3abca}-OH_{glu} and S_{3acca}-Peroxide, respectively. PT-ET process for [S_{3acca}(R)-Peroxide (3443) + Tyr-O•] provides the [S_{4abca}(R)-Peroxide (4443) + Tyr-OH] before the O_2

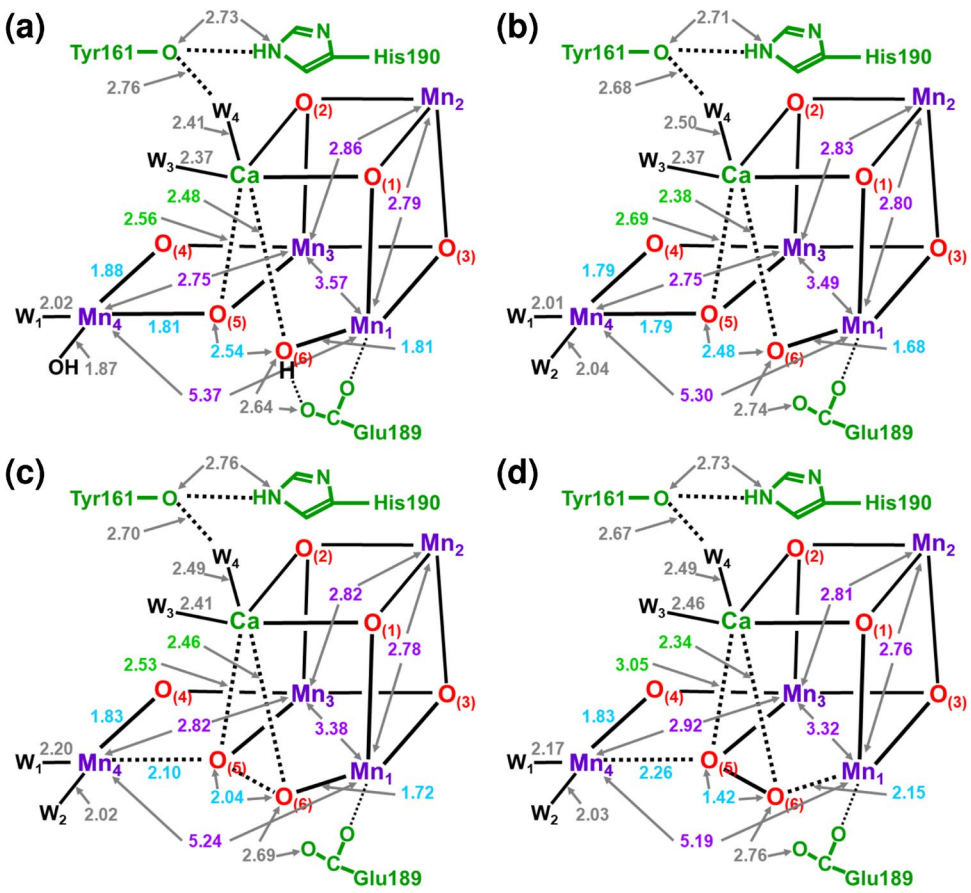

Fig. 8 The optimized geometries of the S_3 + Tyr161-O• radical intermediates by the UB3LYP-D2 method; **a** Mn-hydroxide: [S_{3abca}(R)-OH + Tyr161-O•], **b** Mn-Oxo: [S_{3abca}(R)-Oxo + Tyr161-O•], **c** Mn-Oxyl: [S_{3abca}(R)-Oxyl + Tyr161-O•], and **d** Mn-Peroxide: [S_{3abca}(R)-Peroxide + Tyr161-O•]

evolution [113, 118]. The Ca-$O_{(5)}$ and Ca-$O_{(6)}$ distances for the Mn-Peroxide are 2.34 and 3.05 Å, respectively, indicating the space for the next water insertion at the $O_{(5)}$ site in oxygen evolution [113].

The optimized Mn_1-$O_{(6)}$, Mn_4-$O_{(5)}$, and $O_{(5)}$-$O_{(6)}$ distances for [S_{3acca}(R)-Oxo (Oxyl) + Tyr-O•] are 1.68 (1.72), 1.79 (2.10), and 2.48 (2.04) Å, respectively. The Mn_1-$O_{(6)}$ distance for [S_{3acca}(R)-Oxo + Tyr-O•] is shorter than 1.7 Å, which accord with the Mn(IV) = O distance without the JT effect. The Ca-$O_{(6)}$ distance is 2.38 Å, indicating the strong coordination effect of the $O_{(6)}$ site of $Mn_1 = O_{(6)}$ double bond. The Mn_1-$O_{(6)}$ and Ca-$O_{(6)}$ distances for Mn-Oxyl intermediates are 1.72 and 2.46 Å, respectively, indicating the large reduction of the oxyl-radical character with the Ca-coordination. The $O_{(5)}$-$O_{(6)}$ distance for the Mn-Oxo intermediate is about 2.5 Å, whereas it becomes about 2.0 Å coincide with the SFX-XFEL result [116–119], indicating no O–O bond formation.

The O–O• distance between Tyr-O• and W4 (W7) was calculated to be 2.7 (2.8), indicating the strong hydrogen bond which fixes the harmful radical site of Tyr161. The W7, W6, W5, and W3 form the four-membered ring, which is linked with Cl1 channel (W2-W9-W8-Asp61-…) through the hydrogen bond between W5 and W2 as shown in Fig. 8 [20]. The ring is also linked with O1-channel via the hydrogen bond network W3-W4-W10-…). Therefore, the large QM model (283 atoms) works well for geometry optimizations of the hydrogen bond networks around the $CaMn_4O_x$ cluster in the early S_4 state.

5.3 Comparison between the relative energy by DFT and CC

The optimized geometries of the [S_3 + Tyr-O• (H^+-His190)] configurations are reliable enough for the one-point calculations by UB3LYP/def2-TZVPP computation for elucidation of the relative energies among the possible S_3 intermediates. However, post BS-DFT, namely one-point UHF CCSD(T) computation in Fig. 3 [31, 35] is still difficult in our computer system because very long time CPU is necessary for the systems. Therefore, we have employed its practical and efficient approximate version, namely UCCSD(T) method using DLPNO developed by Neese's group [68, 69]. To this end, we have used the DLPNO consisted of the localized natural orbitals (LNO) obtained by the natural orbital (NO) analysis of the UB3LYP solutions [70–72]. Here, the DLPNO (LNO) CCSD(T_0) method with def2-TZVPP basis in COSMO environment are performed for the four optimized geometries in Fig. 8.

The relative energies between Mn-OH and Mn-Peroxide with Tyr161-O radical are about 16.9, 16.1, and 10.1 kcal/mol, respectively, by UB3LYP, UB3LYP-D2, and DLPNO-CCSD(T_0) methods, respectively. DLPNO-CCSD(T_0) method predicts the formation of the O–O bond even in the [Mn-Peroxide + Tyr161-O radical] state. The energy differences between Mn-OH and Mn-Oxo(Oxyl) are 7.9 (5.3), 9.8 (13.8), and 4.3 (13.0) kcal/mol, respectively, by above three computational methods. Interestingly, UB3LYP predicts the greater stability of the [Mn-Oxyl + Tyr-O radical] state than [Mn-Oxo + Tyr-O radical] state. On the other hand, DLPNO-CCSD(T_0) predicts the reverse tendency. The relative energy is consistent with the geometric information by SFX-XFEL [118]. This indicates a possible reaction pathway in the S_4 state: Mn(IV)-OH → proton transfer → Mn(IV)-Oxo → Mn-Peroxide even during the living state of the Tyr161-O radical, namely formal (5444) valence state; Mn(V) = O bond or •Mn(IV)-O• is not necessary for the O–O bond formation. DLPNO-CCSD(T_0) and UB3LYP results provide quite different conclusions in the S_4 step as illustrated in Fig. 10 (see later). Interestingly, this tendency is also consistent with recent conclusion for the oxygen reduction by C*c*O, where Fe(V) = O is not necessary because of the participation of Tyr244-O• radical as shown in Fig. 11 (see later) [3, 4].

6 Structure and bonding of the PM intermediate in the C*c*O system

6.1 Oxygen reduction mechanism revealed for C*c*O by recent investigations

Over past decades, the oxygen reduction processes in cytochrome *c* oxidase (C*c*O) have been investigated extensively [4, 5, 9, 16, 19, 120–136], indicating several key intermediates denoted as A, P, F, O, E, etc. as shown in Fig. 11: A state is the initial oxygen-inserted state into the Fe(II).. Cu(I) site [9]; P is the O–O bond dissociation step involving Fe(IV) = O bond [9]. The XRD experiments elucidated the 3D structures of C*c*O [123, 124]. DFT computations [127, 129] were performed for Fe–O-O-Cu and Fe-OOH-Cu in C*c*O based on the XRD results [9, 123]. Many investigations have been performed on the structure, bonding and reactivity of C*c*O [9, 16, 19, 120–136]. Here, the subject for this paper is limited to possible roles of Tyr-244 for the oxygen reduction reaction in C*c*O.

Blomberg [133] performed extensive UB3LYP-D3 computations [131] to elucidate relative energies of A, P, F, O, and E states, providing the potential energy diagrams for the oxygen reduction reaction in C*c*O. From the computational results, the most oxidized state is concluded to be the P_M state given in Eq. (15) consisted of Fe(IV) = O and Tyr-O radical instead of Fe(V) = O proposed in early papers [9]. The Fe(IV) = O bond in C*c*O was already detected by time-resolved Raman spectroscopy [121, 122, 126]. Participation of Tyr244 to the O–O bond dissociation was also suggested on the experimental grounds [9, 125]. Recently, Jose et al. [132] performed the magnetic circular dichroism (MCD) experiments for P_M state, supporting the participation of Tyr244-O radical. Thus, the early proposals [9] have been supported by recent extensive investigations [134–136], providing reliable information to examine similarity between reaction cycles in C*c*O and PSII under investigation.

6.2 Electronic structure of the PM intermediate in the C*c*O system

As an extension of previous work on C*c*O [127, 129], full geometry optimization of the large QM model for the P_M state has been performed to elucidate its structure and bonding as shown in Fig. 9. The optimized Fe(IV)-Cu(II) distance was 4.33 Å. The optimized Fe(IV) = O_a and Cu(II)-O_b bond lengths were 1.64 and 1.91 Å, respectively, which compatible with SFX XFEL results [135, 136]. The O_a-O_b distance was 2.80 Å, indicating the hydrogen bond; O_a…H-O_b. On the other hand, the O–O distance between O-radical site of Tyr244 and HO-group of chlorophyll was 2.71 Å, indicating the strong hydrogen bonding to fix the harmful oxygen-radical site.

Spin density (SD) populations for the P_M state are obtained at the optimized geometry. The SD populations are

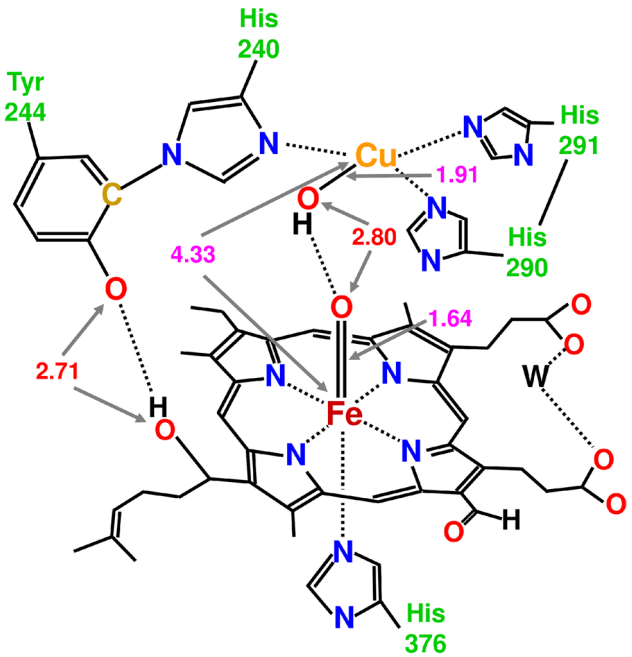

Fig. 9 The optimized geometry of the quantum mechanical QM model (288 atoms) for the P_M configuration of cytochrome c oxidase (C*c*O) with UB3LYP-D2 method with def2-TZVP basis method

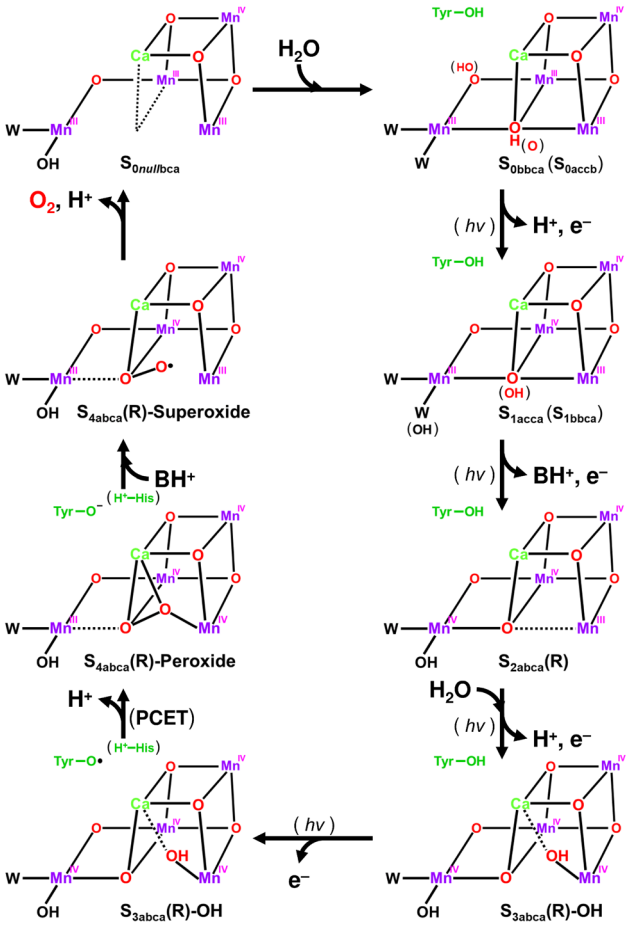

Fig. 10 Possible intermediates structures for the Kok cycle for water oxidation on the basis of the computational results by the DLPNO CCSD(T_0) methods. Tyr-O radical participates the O–O bond formation via the PCET process from S_{3abca}(R)-OH to S_{3acca}(R)-Peroxide. Proton assumed to be not released in the S_1 to S_2 transition, indicating the proton-trapping by a base (B) site near $CaMn_4O_5$ cluster. However, the present QM model is still insufficient for examination of the BH^+ site, indicating the necessity of more extended QM models for the purpose

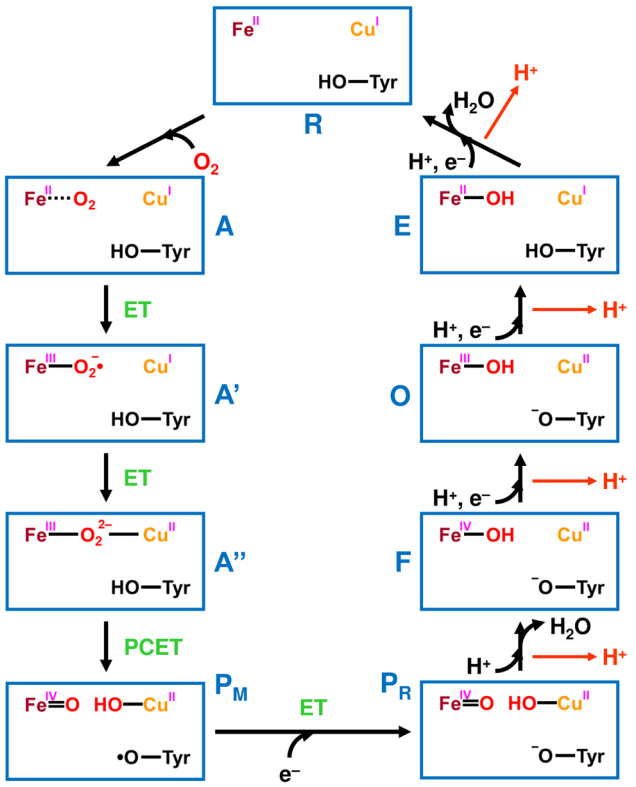

Fig. 11 Possible intermediates for reduction processes of molecular oxygen into water molecule in the cytochrome *c* oxidase (C*c*O) on the basis of available experimental and computational results [9, 16, 19, 120, 121–136]. The O–O bond heterolysis via PCET from A" to P_M becomes feasible with the participation of Tyr244-O radical. Four protons are transferred from the N-site to the P-site in the oxygen reduction process in C*c*O

1.386 and 0.695 for Fe and O sites for Fe(IV) = O, respectively, indicating triplet ground state. They are − 0.168 and − 0.613 for O and Cu sites for HO-Cu(II), respectively, indicating partial spin delocalization. Total spin densities are − 0.917 for Tyr244-O radical and − 0.097 for porphyrin ligand, respectively. Therefore, the spin structure P_M structure is given by the up-up-down-down configuration, indicating the total singlet ground state, which accord with the MCD experimental results [132]: ↑Fe(IV) = O↑… HO-Cu(II)↓…↓O-Tyr244. Thus, BS computational results for the C*c*O model in Fig. 12 provide fundamental information for examination of two sides of the coin relation between oxygen evolution in PSII and oxygen reduction in C*c*O.

7 Discussions

7.1 Reaction cycle for water reduction in cytochrome *c* oxidase

Experimental evidence [116–118] for the S_3 to S_0 transition though transient [S_4] state for oxygen evolution is not conclusive yet although our theoretical computations provide the most probable reaction pathway as illustrated in Fig. 10, where the notation of B is used for a base site for proton trapping in the S_1 to S_2 transition without proton release. On the other hand, spectroscopic and computational results [3, 4, 9, 16, 19, 120–136] for the reaction intermediates in oxygen reduction in cytochrome *c* oxidase (C*c*O) are available. As shown in Fig. 1, C*c*O is consisted of four redox-active transition metal ions (Cu_A, Fe_a, Fe_{a3}, and Cu_B). C*c*O catalyzes reverse reaction of water oxidation in Eq. (1), namely reduction of molecular oxygen into two water molecules: $O_2 + 4H^+ + 4e^- \rightarrow 2H_2O$ [3, 4, 9, 16, 19, 120–136]. Therefore, formal reverse analogy [20] is conceivable between PSII [1, 2] and C*c*O [3, 4] from the viewpoint

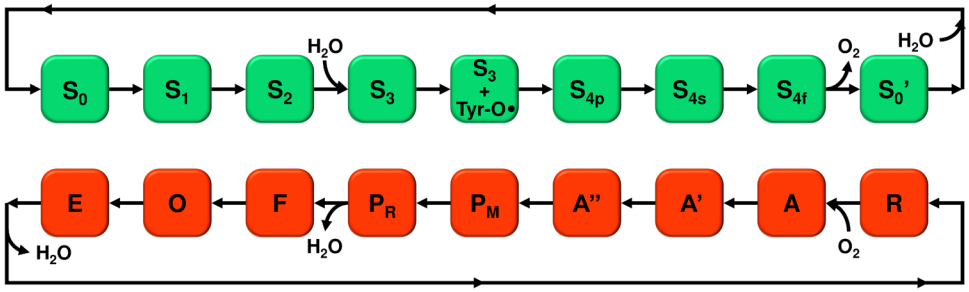

Fig. 12 The formal correspondence between the oxygen evolution from two waters in PSII and the oxygen reduction of molecular oxygen into two waters in C*c*O. Tyrosine 161 and 244 play important roles in these four-electron oxidation and reduction processes in PSII and C*c*O, respectively, indicating no formation of the high-valent Mn(V)=O and Fe(V)=O bonds. The notations of the intermediates are given in Figs. 10 and 11

of the functional behaviors although the constructions of the reaction sites are different between them.

Judging from available experimental results, Heme Fe_{a3} and Cu_B sites of C*c*O for oxygen reduction are regarded as the $Mn_{4(a)}$ and $Mn_{1(d)}$ sites of PSII for water oxidation as shown in Fig. 1. Similarly, Tyr244 and His240 of C*c*O in Fig. 11 are regarded as Tyr161 and His190 of PSII, exhibiting an important proton-coupled electron transfer (PCET) reaction via a water molecule coupled with Tyr244 [9, 16, 19, 120–136]. Three proton insertion pathways, K-, D-, and H-pathways [4], have been proposed for C*c*O, whereas three proton release pathways: path I (Cl1-channel), path II (Y_Z-channel), and path III (O_4-channel), have been proposed for PSII as shown in Fig. 8 [20]. The oxygen insertion and water release pathways are also proposed for C*c*O. On the other hand, oxygen release and water input pathways are proposed for PSII [20, 87, 113, 115]. Thus, C*c*O and PSII have biomolecular systems structures for oxygen (four electron) reduction and water (four electron) oxidation, respectively.

7.2 Possible roles of Tyr244 of C*c*O and Tyr161 of PSII

The most plausible cycle of oxygen reduction in C*c*O is conceivable on the basis of available results [9, 16, 19, 120–136] as illustrated in Fig. 11. The initial state (Reactant state; R) of the oxygen reduction in C*c*O is expressed by Eq. (16).

$$\mathrm{R}: \quad \mathrm{Fe(II)_{a3} \ldots Cu(I)_B} + \mathrm{Tyr244\text{-}OH} \tag{16}$$

where the R state corresponds to S_0' in the Kok cycle for water oxidation which is the S_0 state: $S_{0nullbca}$ (no oxygen at the X site) formed after release of molecular oxygen before second water insertion to afford the S_0 state (S_{0bbca}) in the Kok cycle for water oxidation in Fig. 11. Molecular oxygen is inserted into the resting (R)-state, providing the A state of C*c*O, which is an exchange coupled state between Fe(II) and O_2 as in the case of myoglobin [1, 2]. The A' state with superoxide anion [127] is formed by the one electron transfer (OET) from $Fe(II)_{a3}$ to O–O. Further OET from $Cu(I)_B$ to the O–O anion provides the A'' state with oxygen dianion, namely peroxide formation, on the theoretical ground [127–129]. Spectroscopic results have not been obtained for the A'' state of C*c*O in Fig. 11.

$$\mathrm{A}: \quad \mathrm{Fe(II)_{a3}O\text{-}O \ldots Cu(I)_B} + \mathrm{Tyr244\text{-}OH} \tag{17a}$$

$$A': \quad \mathrm{Fe(III)_{a3}\text{-}OO\bullet \ldots Cu(I)_B} + \mathrm{Tyr244\text{-}OH} \tag{18a}$$

$$A'': \quad \mathrm{Fe(III)_{a3}\text{-}O\text{-}O^{2-}\text{-}Cu(II)_B} + \mathrm{Tyr244\text{-}OH} \tag{19a}$$

The A state is in turn regarded as the final S_{4f} state before O_2 release, S_{4abca}-molecular oxygen (O_2) with the (3433) valence state in the Kok cycle for water oxidation in PSII. The A' state in Fig. 11 is regarded as the intermediate; S_{4abca}-superoxide anion (O_2^-) with the (3443) valence state in Fig. 10. The A'' state in Fig. 11 is regarded as the S_4 state after peroxide bond formation; S_{4abca}-peroxide with the (4443) valence state. Thus, one to one correspondence is feasible for A of C*c*O in Fig. 11 and S_4 for PSII in Fig. 10.

$$\mathrm{S_{4abca}(R)\text{-}O_2(3433)}: \quad \mathrm{[Mn(III)_4Mn(III)_3 - \bullet O\text{-}O\bullet Mn(III)_1]} + \mathrm{Tyr161\text{-}OH} \tag{17b}$$

$$\mathrm{S_{4bcca}(R)\text{-}O_2\ anion\ (3443)} \quad \mathrm{:[Mn(III)_4Mn(IV)_3\text{-}O\text{-}O\bullet Mn(III)_1]} + \mathrm{Tyr161\text{-}OH} \tag{18b}$$

$$\mathrm{S_{4bcca}(R)\text{-}O_2\ dianion\ (4443)}: \quad \mathrm{[Mn(III)_4Mn(IV)_3\text{-}O\text{-}O\text{-}Mn(III)_1]} + \mathrm{Tyr161\text{-}OH} \tag{19b}$$

The next step is the O–O bond fission by the protonation of the oxygen dianion, suggesting the protonated hydroperoxide anion coordinated to [Fe(III)$_{a3}$-OOH Cu(II)-Tyr244-O$^-$] [16, 127–129, 131] namely putative A''' state which has not been observed by experiments. On the other hand, the iron oxo Fe(IV) = O bond has been observed by the Raman spectroscopy in the next P_M stage [121, 122, 126], supporting the participation of Tyr244 anion for the O–O bond heterolysis; namely [Fe(IV) = O HO-Cu(II) Tyr244-O•] in Eq. (21a). Thus, the formation of $[Fe(V)_{a3} = O]^{3+}$ bond is not necessary if the Tyr244-O• radical is participated for the O-OH dissociation reaction as shown in Eq. (20a). Recent interplay between HDFT computation and MCD experiment [132] has also confirmed the participation of tyrosine-radical.

The one ET to P_M provides the reduced configuration P_R in Eq. (23a) (see Fig. 11). Proton addition to P_R provide water molecule, which is released to provide the F intermediate in C*c*O in Eq. (24a). The proton-coupled electron transfer (PC-ET) to the intermediate F provides the intermediate O in Eq. (25a). Further, PC-ET reaction to the intermediate O provides water molecule which is released to recover the initial R state in Eq. (16).

$$A''' : \text{Fe(III)}_{a3}\text{-O-OH} \ldots \text{Cu(II)}_B + \text{Tyr244-O}^- \quad (20a)$$

$$P_M : [\text{Fe(IV)}_{a3} = O^{2+-}\text{HO-Cu(II)}_B] + \text{Tyr244-O•}] \quad (21a)$$

$$P'_M : [\text{Fe(V)}_{a3} = O^{3+-}\text{HO-Cu(II)}_B] + \text{Tyr244-OH} \quad (22a)$$

$$P_R : [\text{Fe(IV)}_{a3} = O^{2+-}\text{HO-Cu(II)}_B] + \text{Tyr244-O}^- \quad (23a)$$

$$F : \left[\text{Fe(IV)}_{a3} = O^{2+}\text{Cu(II)}_B\right] + \text{Tyr244-O}^- \quad (24a)$$

$$O : \left[\text{Fe(III)}_{a3}\text{-OH}^{1+}\text{Cu(II)}_B\right] + \text{Tyr244-O}^- \quad (25a)$$

$$E : \left[\text{Fe(III)}_{a3}\text{OH}^{1+}\text{Cu(I)}_B\right] + \text{Tyr244-OH} \quad (26a)$$

The spectroscopic and computational results for the O–O bond fission in C*c*O provide significant information for the reverse O–O bond formation for water oxidation in PSII. The P_M stage in Eq. (21a) corresponds to the S_3 state with (4444) and Tyrosine radical [$S_{3abca(R)}$-OH + Tyr161-O•] formed (see Fig. 8a) in the third flash in OEC of PSII. On the other hand, the P_M' stage in Eq. (22a) corresponds to the S_{4abca}(R)-OH with (4445) state after one electron transfer to Tyr-O• radical to form formal Mn(V) = O bond in Eq. (22b) where Tyr-O$^-$ is recovered to Tyr-OH via back PT from H$^+$His190 in OEC of PSII. The nucleophilic attack of OH anion to Mn(V) = O provides the Mn(III)-OOH bond as illustrated in Eq. (23b). On the other hand, the one ET to Tyr-O• radical in (23b) provides the S_{3bcca}-OH in Eq. (24b) (see Fig. 6), and the successive proton transfer to S_{3bcca}-OH provides water molecule which is released to give the S_{2abca} state in Eq. (25b). The PC-ET reaction to S_{2abca} state in Eq. (23b) affords the S_{1bbca} state in Eq. (26b). Further PC-ET reaction to S_{1bbca} state provides S_{0bcca} state in Eq. (26b), which is formally converted into $S_{0nullcca}$ state with the release of water molecule in Eq. (27).

$$S_{3abca}\text{(R)-OOH(3444)} : [\text{Mn(III)}_4\text{Mn(IV)}_3\text{-O-OH} \ldots \text{Mn(IV)}_1] + \text{Tyr161-OH} \quad (20b)$$

$$S_{3bcca}\text{(R)(4444)} + \text{Tyr-O•} : \left[\text{Mn(IV)}_4\text{Mn(IV)}_3 = \text{O HO-Mn(IV)}_1\right] + \text{Tyr161-O•} \quad (21b)$$

$$S_{4bcca}\text{(R)(4445)} + \text{Tyrosine} : [\text{Mn(V)}_4\text{Mn(IV)}_3 = \text{OHO-Mn(IV)}_1] + \text{Tyr161-OH} \quad (22b)$$

$$S_{3bcca}\text{(R)(4444)} + \text{Tyr} - \text{OH} : [\text{Mn(IV)}_4\text{Mn(IV)}_3 = \text{OHO-Mn(IV)}_1] + \text{Tyr161-OH} \quad (23b)$$

$$S_{2bcca}\text{(R)(3444)} + \text{Tyr} - \text{OH} : \left[\text{Mn(IV)}_4\text{Mn(IV)}_3 = \text{OMn(III)}_1\right] + \text{Tyr161-OH} \quad (24b)$$

$$S_{1bbca}\text{(R)(3443)} + \text{Tyr-OH} : \left[\text{Mn(III)}_4\text{Mn(IV)}_3\text{-OHMn(III)}_1\right] + \text{Tyr161-OH} \quad (25b)$$

$$S_{0bcca}\text{(R)(3433)} + \text{Tyr-OH} : \left[\text{Mn(III)}_4\text{Mn(III)}_3\text{-OHMn(III)}_1\right] + \text{Tyr161-OH} \quad (26b)$$

$$S_{0bcca}\text{(R)(3433)} + \text{Tyr-OH:} \left[\text{Mn(III)}_4\text{Mn(III)}_3\text{Mn(III)}_1\right] + \text{Tyr161-OH} \quad (27)$$

Four electron reduction of molecular oxygen to two water molecules occurs by using two electrons from Fe(II)$_{a3}$, one electron from Cu(I)$_A$ and one electron from Tyr244 in the Tyr244-radical assisted O–O dissociation of C*c*O. Proton-coupled electron-transfer (PC-ET) processes play important roles as illustrated in Fig. 5, indicating no formation of high-valent Fe(V) = O bond. On the other hand, four-electron oxidation of two water molecules into molecular oxygen occurs by using three electrons from $CaMn_4O_x$ cluster and one electron from Tyr161-OH. As illustrated in Fig. 5 [20], the PC-ET processes indicate no formation of high-valent Mn(V) = O bond. Thus, one-to-one correspondences are found to be operative in oxygen reduction in C*c*O and oxygen evolution in PSII. Four photon energies (4*hν*)

are required for the up-hill reactions for water oxidations to molecular oxygen in Fig. 10. On the other hand, downhill reactions of molecular oxygen to water molecules in C*c*O provides driving forces for four proton releases from N-side to P-side as shown in Fig. 11, and four protons in P-side are used to afford ATP from ADP. Finally, we have depicted whole analogy [12–16] between water oxidation on PSII and oxygen reduction in C*c*O in Fig. 12.

7.3 Bio-inspired artificial systems

Elucidation of the mechanism of natural water oxidation in PSII is expected to provide guiding principles for design and construction of bio-inspired artificial systems for water oxidation [20, 84]. According to the reaction cycles in Figs. 10, 11, 12, tyrosine group play an important role for water oxidation in PSII and oxygen reduction in C*c*O. Wada et al. [137] has already achieved the water oxidation with the bio-inspired artificial Ru-oxo species with electron acceptor ligands, indicating the participation of phenoxy radical, quinone, etc. for the O–O bond formation [137, 138]. The iso-spin analogy [138] between the $CaMn_4O_x$ cluster and the artificial Ru catalyst [137] has been also elucidated based on the spin Hamiltonian model. The HDFT computations [139] have elucidated the detailed mechanism of water oxidation with participation of quinone ligand in the Ru catalysts [137].

Very recently, Kumagai et al. [140] have investigated the water oxidation with the Ru catalyst ligated with phenol group. Their detailed experiments have provided reliable information that the phenoxy radical participates in the O–O bond formation for water oxidation in contradiction to the conventional acid–base (AB) mechanism in Eq. (7b) and radical coupling (RC) mechanism in Eq. (7a). They have pointed out that their results are consistent with the phenoxy-radical participated mechanism, for example proton coupled electron transfer (PCET) [141] or the non-adiabatic (NA) one-ET mechanism for water oxidation [142]. Thus, similar mechanisms can be expected for water oxidation by 3d transition metal oxo systems with radical ligands [143, 144].

8 Concluding remark

In this paper, fundamental concepts and computational procedures for broken-symmetry (BS) and post BS methods are summarized for theoretical modeling and designs of photo-induced bio-inspired catalysts for oxygen evolution reaction (OER) and oxygen reduction reaction (ORR). The PT and ET processes in water oxidation in PSII and oxygen reduction in C*c*O were examined in detail with synergetic combinations of available experimental results such as time-resolved SFX XFEL experiments [17, 18, 116–119] and recent computational results involving DLPNO-CCSD(T_0) computational results, elucidating the quantum similarity between these reactions. Three electrons in metal sites and one electron in tyrosine radical site were found to be operative in four electron oxidation–reduction processes in these enzymes in Fig. 1, indicating plausible conclusion of no formation of the high valent Mn(V) = O and Fe(V) = O because of the PC-ET processes with hydrogen bonds networks including tyrosine. Available time-resolved SFX-XFEL for the $S_3 \rightarrow [S_4] \rightarrow S_0$ transition in OEC of PSII [116–118] were consistent with such a new picture in biological systems in contrast to artificial systems without such environmental effects.

Elucidation of the possible mechanism of natural water oxidation in Fig. 10 [20, 118] provides guiding principle for design and construction of artificial water oxidation catalysts for which ligated organic radical(s) participates in the O–O bond formation. Very recently, the Ru catalyst ligated with phenoxy radical [140] has been found to undergo the water oxidation where the ligated radical also participates in the O–O bond formation. Four holes necessary for water oxidation into molecular oxygen are stored in both metal sites and organic radical site(s) in these artificial systems without large over-potentials [137–140]. Present theoretical analysis is expected to provide bio-inspired guiding principle for developments of earth-abundant artificial systems with photo-induced four holes for water oxidation [143–145].

Supplementary Information The online version contains supplementary material available at https://doi.org/10.1007/s43630-024-00648-w.

Acknowledgements We thank referees for their careful, critical, and helpful comments for this manuscript. We also thank the editor for helpful advice. One of the authors (KY) thanks Prof. S. Yoshikawa and Prof. T. Tsukihara for helpful discussions on the structure and bonding in C*c*O, and Dr. K. Kawakami for his kind discussions on the structure and bonding of the $CaMn_4O_x$ cluster in PSII. This work has been supported with MEXT KAKENHI Grant Number JP20H05453 (MS), JP22K05317 (HI), and JP22H04916 (MS, KY). Numerical calculations were carried out under the supports of Research Center for Computational Science, Okazaki, Japan (23-IMS-C023 and 24-IMS-C023) and supercomputer Fugaku provided by the RIKEN Center for Computational Science, Kobe, Japan (Project ID: hp240186).

Funding Open Access funding provided by Osaka University.

Data availability The datasets analysed during the current study are available from the corresponding author on reasonable request.

Declarations

Conflict of interest The authors declare that they have no conflict of interest.

References

1. Wydrzynski, T. J., & Satoh, K. (2005). *Photosystem II: The light-driven water: plastoquinone oxidoreductase, advances in photosynthesis and respiration* (Vol. 22). Springer.
2. Shen, J.-R., Satoh, K., & Allakhverdiev, S. I. (2021). *Photosynthesis: Molecular approaches to solar energy conversion, advances in photosynthesis and respiration* (Vol. 47). Springer.
3. Wikström, M., Krab, K., & Sharma, V. (2018). Oxygen activation and energy conservation by cytochrome *c* oxidase. *Chemical Reviews, 118*, 2469–2490. https://doi.org/10.1021/acs.chemrev.7b00664
4. Yoshikawa, S., & Shimada, A. (2015). Reaction mechanism of cytochrome *c* oxidase. *Chemical Reviews, 115*, 1936–1989. https://doi.org/10.1021/cr500266a
5. Solomon, E. I., Sundaram, U. M., & Machonkin, T. E. (1996). Multicopper oxidases and oxygenases. *Chemical Reviews, 96*, 2563–2606. https://doi.org/10.1021/cr950046o
6. Solomon, E. I., Heppner, D. E., Johnston, E. M., Ginsbach, J. W., Cirera, J., Qayyum, M., Kieber-Emmons, M. T., Kjaergaard, C. H., Hadt, R. G., & Tian, L. (2014). Copper active sites in biology. *Chemical Reviews, 114*, 3659–3853. https://doi.org/10.1021/cr400327t
7. Zouni, A., Witt, H.-T., Kern, J., Fromme, P., Krauss, N., Saenger, W., & Orth, P. (2001). Crystal structure of photosystem II from *Synechococcus elongatus* at 3.8 Å resolution. *Nature, 409*, 739–743. https://doi.org/10.1038/35055589
8. Umena, Y., Kawakami, K., Shen, J.-R., & Kamiya, N. (2011). Crystal structure of oxygen-evolving photosystem II at a resolution of 1.9 Å. *Nature, 473*, 55–60. https://doi.org/10.1038/nature09913
9. Tsukihara, T., Aoyama, H., Yamashita, E., Tomizaki, T., Yamaguchi, H., Shinzawa-Itoh, K., Nakajima, R., Yaono, R., & Yoshikawa, S. (1995). Structures of metal sites of oxidized bovine heart cytochrome *c* oxidase at 2.8 Å. *Science, 269*, 1069–1074. https://doi.org/10.1126/science.7652554
10. Wikström, M., & Sharma, V. (2018). Proton pumping by cytochrome *c* oxidase—A 40 year anniversary. *Biochimica et Biophysica Acta - Bioenergetics, 1859*, 692–698. https://doi.org/10.1016/j.bbabio.2018.03.009
11. Hirata, K., Shinzawa-Itoh, K., Yano, N., Takemura, S., Kato, K., Hatanaka, M., Muramoto, K., Kawahara, T., Tsukihara, T., Yamashita, E., Tono, K., Ueno, G., Hikima, T., Murakiami, H., Inubushi, Y., Yabashi, M., Ishikawa, T., Yamamoto, M., Ogura, T., … Ago, H. (2014). Determination of damage-free crystal structure of an X-ray–sensitive protein using an XFEL. *Nature Methods, 11*, 734–736. https://doi.org/10.1038/nmeth.2962
12. Hoganson, C. W., Pressler, M. A., Proshlyakov, D. A., & Babcock, G. T. (1998). From water to oxygen and back again: Mechanistic similarities in the enzymatic redox conversion between water and dioxygen. *Biochimica et Biophysica Acta - Bioenergetics, 1365*, 170–174. https://doi.org/10.1016/S0005-2728(98)00057-7
13. Wikström, M., & Verkhovsky, M. I. (2006). Towards the mechanism of proton pumping by the haem-copper oxidases. *Biochimica et Biophysica Acta - Bioenergetics, 1757*, 1047–1051. https://doi.org/10.1016/j.bbabio.2006.01.010
14. Silverstein, T. P. (2011). Photosynthetic water oxidation vs. mitochondrial oxygen reduction: Distinct mechanistic parallels. *Journal of Bioenergetics and Biomembranes, 43*, 437–446. https://doi.org/10.1007/s10863-011-9370-7
15. Gunner, M. R., Amin, M., Zhu, X., & Lu, J. (2013). Molecular mechanisms for generating transmembrane proton gradients. *Biochimica et Biophysica Acta - Bioenergetics, 1827*, 892–913. https://doi.org/10.1016/j.bbabio.2013.03.001
16. Blomberg, M. R. A. (2016). Mechanism of oxygen reduction in cytochrome *c* oxidase and the role of the active site tyrosine. *Biochemistry, 55*, 489–500. https://doi.org/10.1021/acs.biochem.5b01205
17. Kern, J., Chatterjee, R., Young, I. D., Fuller, F. D., Lassalle, L., Ibrahim, M., Gul, S., Fransson, T., Brewster, A. S., Alonso-Mori, R., Hussein, R., Zhang, M., Douthit, L., de Lichtenberg, C., Cheah, M. H., Shevela, D., Wersig, J., Seuffert, I., Sokaras, D., … Yachandra, V. K. (2018). Structures of the intermediates of Kok's photosynthetic water oxidation clock. *Nature, 563*, 421–425. https://doi.org/10.1038/s41586-018-0681-2
18. Suga, M., Akita, F., Yamashita, K., Nakajima, Y., Ueno, G., Li, H., Yamane, T., Hirata, K., Umena, Y., Yonekura, S., Yu, L. J., Murakami, H., Nomura, T., Kimura, T., Kubo, M., Baba, S., Kumasaka, T., Tono, K., Yabashi, M., … Shen, J. R. (2019). An oxyl/oxo mechanism for oxygen-oxygen coupling in PSII revealed by an x-ray free-electron laser. *Science, 366*, 334–338. https://doi.org/10.1126/science.aax6998
19. Shimada, A., Kubo, M., Baba, S., Yamashita, K., Hirata, K., Ueno, G., Nomura, T., Kimura, T., Shinzawa-Itoh, K., Baba, J., Hatano, K., Eto, Y., Miyamoto, A., Murakami, H., Kumasaka, T., Owada, S., Tono, K., Yabashi, M., Yamaguchi, Y., Yanagisawa, S., Sakaguchi, M., Ogura, T., Komiya, R., Yan, J., Yamashita, E., Yamamoto, M., Ago, H., Yoshikawa, S., & Tsukihara, T. (2017). A nanosecond time-resolved XFEL analysis of structural changes associated with CO release from cytochrome c oxidase. *Science Advances*, 3, e1603042 (2017). https://doi.org/10.1126/sciadv.1603042
20. Yamaguchi, K., Miyagawa, K., Shoji, M., Kawakami, T., Isobe, H., Yamanaka, S., & Nakajima, T. (2023). Theoretical elucidation of the structure, bonding, and reactivity of the $CaMn_4O_x$ clusters in the whole Kok cycle for water oxidation embedded in the oxygen evolving center of photosystem II. New molecular and quantum insights into the mechanism of the O–O bond formation. *Photosynthesis Research*. https://doi.org/10.1007/s11120-023-01053-7. In press.
21. Miyagawa, K., Shoji, M., Isobe, H., Yamanaka, S., Kawakami, T., Okumura, M., & Yamaguchi, K. (2020). Theory of chemical bonds in metalloenzymes XXIV electronic and spin structures of FeMoco and Fe-S clusters by classical and quantum computing. *Molecular Physics, 118*, e1760388. https://doi.org/10.1080/00268976.2020.1760388
22. Thouless, D. J. (1960). Stability conditions and nuclear rotations in the Hartree-Fock theory. *Nuclear Physics, 21*, 225–232. https://doi.org/10.1016/0029-5582(60)90048-1
23. Čížek, J., & Paldus, J. (1967). Stability conditions for the solutions of the Hartree—Fock equations for atomic and molecular systems. Application to the pi-electron model of cyclic polyenes. *The Journal of Chemical Physics, 47*, 3976–3985. https://doi.org/10.1063/1.1701562

24. Fukutome, H. (1968). Spin density wave and charge transfer wave in long conjugated molecules. *Progress of Theoretical Physics, 40*, 998–1012. https://doi.org/10.1143/PTP.40.998
25. Paldus, J., & Čížek, J. (1970). Stability conditions for the solutions of the Hartree-Fock equations for atomic and molecular systems. II. Simple open-shell case. *The Journal of Chemical Physics, 52*, 2919–2936. https://doi.org/10.1063/1.1673419
26. Coester, F. (1958). Bound states of a many-particle system. *Nuclear Physics, 7*, 421–424. https://doi.org/10.1016/0029-5582(58)90280-3
27. Coester, F., & Kümmel, H. (1960). Short-range correlations in nuclear wave functions. *Nuclear Physics, 17*, 477–485. https://doi.org/10.1016/0029-5582(60)90140-1
28. Čížek, J. (1966). On the correlation problem in atomic and molecular systems. Calculation of wavefunction components in ursell-type expansion using quantum-field theoretical methods. *The Journal of Chemical Physics, 45*, 4256–4266. https://doi.org/10.1063/1.1727484
29. Paldus, J., Čížek, J., & Shavitt, I. (1972). Correlation problems in atomic and molecular systems. IV. Extended coupled-pair many-electron theory and its application to the BH_3 molecule. *Physical Review A, 5*, 50–67. https://doi.org/10.1103/PhysRevA.5.50
30. Bartlett, R. J., & Purvis, G. D. (1978). Many-body perturbation theory, coupled-pair many-electron theory, and the importance of quadruple excitations for the correlation problem. *International Journal of Quantum Chemistry, 14*, 561–581. https://doi.org/10.1002/qua.560140504
31. Yamaguchi, K. (1980). Multireference (MR) configuration interaction (CI) approach for quasidegenerate systems. *International Journal of Quantum Chemistry, 18*, 269–284. https://doi.org/10.1002/qua.560180831
32. Yamaguchi, K. (1975). The electronic structures of biradicals in the unrestricted Hartree-Fock approximation. *Chemical Physics Letters, 33*, 330–335. https://doi.org/10.1016/0009-2614(75)80169-2
33. Takabe, T., & Yamaguchi, K. (1976). Electron-transfer biradical intermediates in ground-state reactions. *Chemical Physics Letters, 40*, 347–352. https://doi.org/10.1016/0009-2614(76)85094-4
34. Yamaguchi, K., Yoshioka, Y., & Fueno, T. (1977). Interrelationships between the effective for the H_3 radical. *Chemical Physics Letters, 46*, 360–365. https://doi.org/10.1016/0009-2614(77)85282-2
35. Yamaguchi, K. (1990). Instability in Chemical Bonds –- SCF, APUMP, APUCC, MR-CI and MR- CC Approaches –-. In R. Carbó & M. Klobukowski (Eds.), *Self-consistent field: Theory and applications* (pp. 727–823). Elsevier.
36. Hubbard, J. (1963). Electron correlations in narrow energy bands. *Proceedings of the Royal Society of London. Series A, 276*, 238–257. https://doi.org/10.1098/rspa.1963.0204
37. Kok, B., Forbush, B., & McGloin, M. (1970). Cooperation of charges in photosynthetic O_2 evolution–I. A linear four step mechanism. *Photochemistry and Photobiology, 11*, 457–475. https://doi.org/10.1111/j.1751-1097.1970.tb06017.x
38. Hoffmann, R., & Woodward, R. B. (1965). Selection rules for concerted cycloaddition reactions. *Journal of the American Chemical Society, 84*, 2046–2048. https://doi.org/10.1021/ja01087a034
39. Woodward, R. B., & Hoffmann, R. (1969). The conservation of orbital symmetry. *Angewandte Chemie International Edition, 8*, 781–853. https://doi.org/10.1002/anie.196907811
40. Hückel, E. (1931). Quantentheoretische beiträge zum benzolproblem I. Die elektronenkonfiguration des benzols und verwandter verbindungen. *Zeitschrift für Physik, 70*, 204–286. https://doi.org/10.1007/BF01339530
41. Hoffmann, R. (1963). An extended Hückel theory. I. Hydrocarbons. *The Journal of Chemical Physics, 39*, 1397–1412. https://doi.org/10.1063/1.1734456
42. Noether, E. (1918). Invariante Variationsprobleme. *Nachrichten von der Gesellschaft der Wissenschaften zu Göttingen, Mathematisch-Physikalische Klasse, 1918*, 235–257.
43. Kanamori, J. (1963). Electron correlation and ferromagnetism of transition metals. *Progress of Theoretical Physics, 30*, 275–289. https://doi.org/10.1143/PTP.30.275
44. Gutzwiller, M. C. (1963). Effect of correlation on the ferromagnetism of transition metals. *Physical Review Letters, 10*, 159–162. https://doi.org/10.1103/PhysRevLett.10.159
45. Shoji, M., Isobe, H., Yamanaka, S., Umena, Y., Kawakami, K., Kamiya, N., Shen, J.-R., Nakajima, T., & Yamaguchi, K. (2015). Chapter seven - Large-scale QM/MM calculations of hydrogen bonding networks for proton transfer and water inlet channels for water oxidation—theoretical system models of the oxygen-evolving complex of photosystem II. In J.R. Sabin, & E.J. Brändas (Eds.), *Advances in Quantum Chemistry* (Volume 70, pp. 325–413). Elsevier. https://doi.org/10.1016/bs.aiq.2014.10.001
46. Roothaan, C. C. J. (1951). New developments in molecular orbital theory. *Reviews of Modern Physics, 23*, 69–89. https://doi.org/10.1103/RevModPhys.23.69
47. Fukui, K. (1982). The role of frontier orbitals in chemical reactions (Nobel lecture). *Angewandte Chemie International Edition, 21*, 801–809. https://doi.org/10.1002/anie.198208013
48. Slater, J. C. (1951). A simplification of the Hartree-Fock method. *Physical Review, 81*, 385–390. https://doi.org/10.1103/PhysRev.81.385
49. Parr, R. G., & Yang, W. (1989). *Density-functional theory of atoms and molecules*. Oxford University Press.
50. Yamaguchi, K. (1979). Singlet unrestricted Hartree-Fock Slater (UHFS) model for unstable metal-metal bonds. *Chemical Physics Letters, 66*, 395–399. https://doi.org/10.1016/0009-2614(79)85043-5
51. Coulson, C. A. (1939). The electronic structure of some polyenes and aromatic molecules. VII. Bonds of fractional order by the molecular orbital method. *Proceedings of the Royal Society of London, Series A, 169*, 413–428. https://doi.org/10.1098/rspa.1939.0006
52. Fujishima, A., & Honda, K. (1972). Electrochemical photolysis of water at a semiconductor electrode. *Nature, 238*, 37–38. https://doi.org/10.1038/238037a0
53. Tsubomura, H., Matsumura, M., Nomura, Y., & Amamiya, T. (1976). Dye sensitised zinc oxide: Aqueous electrolyte: Platinum photocell. *Nature, 261*, 402–403. https://doi.org/10.1038/261402a0
54. Kawai, T., & Sakata, T. (1980). Conversion of carbohydrate into hydrogen fuel by a photocatalytic process. *Nature, 286*, 474–476. https://doi.org/10.1038/286474a0
55. Hashimoto, K., Irie, H., & Fujishima, A. (2005). TiO_2 photocatalysis: A historical overview and future prospects. *Japanese Journal of Applied Physics, 44*, 8269–8285. https://doi.org/10.1143/JJAP.44.8269
56. Yamaguchi, K., & Fueno, T. (1977). Diradical and zwitterionic intermediates in the excited state. *Chemical Physics Letters, 23*, 375–386. https://doi.org/10.1016/0301-0104(77)85063-5
57. Yamaguchi, K., Takada, K., Otsuji, Y., & Mizuno, K. (1992). Theoretical and general aspects of organic peroxides. In W. Ando (Ed.), *Organic peroxides* (pp. 1–100). John Wiley & Sons.
58. Yamaguchi, K. (1985). Theoretical calculations of singlet oxygen reactions. In A. A. Frimer (Ed.), *Singlet O2* (Vol. III, pp. 119–250). CRC Press.

59. Groves, J. T., Haushalter, R. C., Nakamura, M., Nemo, T. E., & Evans, B. J. (1981). High-valent iron-porphyrin complexes related to peroxidase and cytochrome P-450. *Journal of the American Chemical Society, 103*, 2884–2886. https://doi.org/10.1021/ja00400a075
60. Holm, R. H. (1987). Metal-centered oxygen atom transfer reactions. *Chemical Reviews, 87*, 1401–1449. https://doi.org/10.1021/cr00082a005
61. Meunier, B., de Visser, S. P., & Shaik, S. (2004). Mechanism of oxidation reactions catalyzed by cytochrome P450 enzymes. *Chemical Reviews, 104*, 3947–3980. https://doi.org/10.1021/cr020443g
62. Yamaguchi, K., Takahara, Y., & Fueno, T. (1986). Ab-initio molecular orbital studies of structure and reactivity of transition metal-oxo compounds. In V. H. Smith, H. F. Schaefer, & K. Morokuma (Eds.), *Applied quantum chemistry* (pp. 155–184). D. Reidel Pub. Com.
63. Isobe, H., Shoji, M., Shen, J.-R., & Yamaguchi, K. (2016). Chemical equilibrium models for the S_3 state of the oxygen-evolving complex of photosystem II. *Inorganic Chemistry, 55*, 502–511. https://doi.org/10.1021/acs.inorgchem.5b02471
64. Becke, A. D. (1993). A new mixing of Hartree-Fock and local density-functional theories. *The Journal of Chemical Physics, 98*, 1372–1377. https://doi.org/10.1063/1.464304
65. Reiher, M., Salomon, O., & Hess, B. A. (2001). Reparameterization of hybrid functionals based on energy differences of states of different multiplicity. *Theoretical Chemistry Accounts, 107*, 48–55. https://doi.org/10.1007/s00214-001-0300-3
66. Yamaguchi, K., Shoji, M., Isobe, H., Miyagawa, K., & Nakatani, K. (2019). Theory of chemical bonds in metalloenzymes XXII: A concerted bond-switching mechanism for the oxygen–oxygen bond formation coupled with one electron transfer for water oxidation in the oxygen-evolving complex of photosystem II. *Molecular Physics, 117*, 2320–2354. https://doi.org/10.1080/00268976.2018.1552799
67. Löwdin, P.-O. (1955). Quantum theory of many-particle systems. I. Physical interpretations by means of density matrices, natural spin-orbitals, and convergence problems in the method of configurational interaction. *Physical Review, 97*, 1474–1489. https://doi.org/10.1103/PhysRev.97.1474
68. Riplinger, C., Sandhoefer, B., Hansen, A., & Neese, F. (2013). Natural triple excitations in local coupled cluster calculations with pair natural orbitals. *The Journal of Chemical Physics, 139*, 134101. https://doi.org/10.1063/1.4821834
69. Saitow, M., Becker, U., Riplinger, C., Valeev, E. F., & Neese, F. (2017). Natural triple excitations in local coupled cluster calculations with pair natural orbitals. *The Journal of Chemical Physics, 146*, 164105. https://doi.org/10.1063/1.4981521
70. Miyagawa, K., Kawakami, T., Isobe, H., Shoji, M., Yamanaka, S., Nakatani, K., Okumura, M., Nakajima, T., & Yamaguchi, K. (2019). Domain-based local pair natural orbital CCSD(T) calculations of six different S1 structures of oxygen evolving complex of photosystem II. Proposal of multi-intermediate models for the S1 state. *Chemical Physics Letters, 732*, 136660. https://doi.org/10.1016/j.cplett.2019.136660
71. Miyagawa, K., Kawakami, T., Suzuki, Y., Isobe, H., Shoji, M., Yamanaka, S., Okumura, M., Nakajima, T., & Yamaguchi, K. (2021). Relative stability among intermediate structures in S_2 state of $CaMn_4O_5$ cluster in PSII by using hybrid-DFT and DLPNO-CC methods and evaluation of magnetic interactions between Mn ions. *Journal of Photochemistry and Photobiology A: Chemistry, 405*, 112923. https://doi.org/10.1016/j.jphotochem.2020.112923
72. Miyagawa, K., Shoji, M., Isobe, H., Kawakami, T., Nakajima, T., & Yamaguchi, K. (2022). Relative energies among S3 intermediates in the photosystem II revealed by DLPNO coupled cluster and hybrid DFT calculations. Possible pathways of water insertion in the S2 to S3 transition. *Chemical Physics Letters, 793*, 139439. https://doi.org/10.1016/j.cplett.2022.139439
73. Anderson, P. W. (1973). Resonating valence bonds: A new kind of insulator? *Materials Research Bulletin, 8*, 153–160. https://doi.org/10.1016/0025-5408(73)90167-0
74. Yamaguchi, K. (1975). General spin structures of organic radicals. *Chemical Physics Letters, 30*, 288–292. https://doi.org/10.1016/0009-2614(75)80122-9
75. Shores, M. P., Nytko, E. A., Bartlett, B. M., & Nocera, D. G. (2005). A structurally perfect $S = 1/2$ kagomé antiferromagnet. *Journal of the American Chemical Society, 127*, 13462–13463. https://doi.org/10.1021/ja053891p
76. Yamaguchi, K., Yoshioka, Y., Takatsuka, T., & Fueno, T. (1978). Extended Hartree-Fock (EHF) theory in chemical reactions. *Theoretica Chimica Acta, 48*, 185–206. https://doi.org/10.1007/BF00549018
77. Yamaguchi, K., Fueno, T., Ozaki, M., Ueyama, N., & Nakamura, A. (1990). A general spin-orbital (GSO) description of antiferromagnetic spin couplings between four irons in iron-sulfur clusters. *Chemical Physics Letters, 168*, 56–62. https://doi.org/10.1016/0009-2614(90)85102-I
78. Rüttinger, W., & Dismukes, G. C. (1997). Synthetic water-oxidation catalysts for artificial photosynthetic water oxidation. *Chemical Reviews, 97*, 1–24. https://doi.org/10.1021/cr950201z
79. Yoshioka, Y., Kubo, S., Kiribayashi, S., Takano, Y., & Yamaguchi, K. (1998). Hubbard and Heisenberg models for four-site four-electron systems. Group-theoretical interrelationships and applications to multinuclear transition-metal clusters. *Bulletin of the Chemical Society of Japan, 71*, 573–588. https://doi.org/10.1246/bcsj.71.573
80. Yamanaka, S., Yamaki, D., Shigeta, Y., Nagao, H., Yoshioka, Y., Suzuki, N., & Yamaguchi, K. (2000). Generalized spin density functional theory for noncollinear molecular magnetism. *International Journal of Quantum Chemistry, 80*, 664–671. https://doi.org/10.1002/1097-461X(2000)80:4/5%3c664::AID-QUA15%3e3.0.CO;2-C
81. Yamanaka, S., Takeda, R., & Yamaguchi, K. (2003). Density functional study of tetrahedral manganese clusters. *Polyhedron, 22*, 2013–2017. https://doi.org/10.1016/S0277-5387(03)00168-2
82. Takeda, R., Yamanaka, S., Shoji, M., & Yamaguchi, K. (2007). Ab initio calculation of the Dzyaloshinskii-Moriya parameters: Spin–orbit GSO-HF, DFT, and CI approaches. *International Journal of Quantum Chemistry, 107*, 1328–1334. https://doi.org/10.1002/qua.21267
83. Ferreira, K. N., Iverson, T. M., Maghlaoui, K., Barber, J., & Iwata, S. (2004). Architecture of the photosynthetic oxygen-evolving center. *Science, 303*, 1831–1838. https://doi.org/10.1126/science.1093087
84. Isobe, H., Shoji, M., Koizumi, K., Kitagawa, Y., Yamanaka, S., Kuramitsu, S., & Yamaguchi, K. (2005). Electronic and spin structures of manganese clusters in the photosynthesis II system. *Polyhedron, 24*, 2767–2777. https://doi.org/10.1016/j.poly.2005.08.049
85. Takeda, R., Yamanaka, S., & Yamaguchi, K. (2006). Resonating broken-symmetry approach to biradicals and polyradicals. *International Journal of Quantum Chemistry, 106*, 3303–3311. https://doi.org/10.1002/qua.21203
86. Yamanaka, S., Kanda, K., Saito, T., Umena, Y., Kawakami, K., Shen, J.-R., Kamiya, N., Okumura, M., Nakamura, H., & Yamaguchi, K. (2012). Chapter 5 - Electronic and spin structures of the $CaMn_4O_5(H_2O)_4$ cluster in OEC of PSII refined to 1.9 Å X-ray resolution. In J.R. Sabin, & E.J. Brändas (Eds.), *Advances in Quantum Chemistry* (Volume 64, pp.121–187). Elsevier. https://doi.org/10.1016/B978-0-12-396498-4.00016-8

87. Isobe, H., Shoji, M., Yamanaka, S., Umena, Y., Kawakami, K., Kamiya, N., Shen, J.-R., & Yamaguchi, K. (2012). Theoretical illumination of water-inserted structures of the $CaMn_4O_5$ cluster in the S_2 and S_3 states of oxygen-evolving complex of photosystem II: Full geometry optimizations by B3LYP hybrid density functional. *Dalton Transactions, 41*, 13727–13740. https://doi.org/10.1039/c2dt31420g
88. Roos, B. O. (1980). The complete active space SCF method in a fock-matrix-based super-CI formulation. *International Journal of Quantum Chemistry, 18*, 175–189. https://doi.org/10.1002/qua.560180822
89. Langhoff, S. R., & Davidson, E. R. (1974). Configuration interaction calculations on the nitrogen molecule. *International Journal of Quantum Chemistry, 8*, 61–72. https://doi.org/10.1002/qua.560080106
90. Yamaguchi, K. (1979). Configuration interaction (CI), coupled-cluster (CC) and many-body perturbation (MBPT) approaches in the unrestricted Hartree—Fock—Slater (UHFS) model. *Chemical Physics Letters, 68*, 477–482. https://doi.org/10.1016/0009-2614(79)87242-5
91. Mahapatra, U. S., Datta, B., & Mukherjee, D. (1998). A state-specific multi-reference coupled cluster formalism with molecular applications. *Molecular Physics, 94*, 157–171. https://doi.org/10.1080/002689798168448
92. Saito, T., Yasuda, N., Nishihara, S., Yamanaka, S., Kitagawa, Y., Kawakami, T., Okumura, M., & Yamaguchi, K. (2011). Broken-symmetry natural orbital (BSNO)-Mk-MRCC study on the exchange coupling in the binuclear copper(II) compounds. *Chemical Physics Letters, 505*, 11–15. https://doi.org/10.1016/j.cplett.2011.02.018
93. Reiher, M., Wiebe, N., Svore, K. M., Wecker, D., & Troyer, M. (2017). Elucidating reaction mechanisms on quantum computers. *Proceedings of the National Academy of Sciences, 114*, 7555–7560. https://doi.org/10.1073/pnas.1619152114
94. Marcus, R. A. (1993). Electron transfer reactions in chemistry. Theory and experiment. *Reviews of Modern Physics, 65*, 599–610. https://doi.org/10.1103/RevModPhys.65.599
95. Greife, P., Schönborn, M., Capone, M., Assunção, R., Narzi, D., Guidoni, L., & Dau, H. (2023). The electron–proton bottleneck of photosynthetic oxygen evolution. *Nature, 617*, 623–628. https://doi.org/10.1038/s41586-023-06008-5
96. Mulliken, R. S. (1964). The interaction of electron donors and acceptors. *Journal de Chimie Physique, 61*, 20–38. https://doi.org/10.1051/jcp/1964610020
97. Binstead, R. A., Moyer, B. A., Samuels, G. J., & Meyer, T. J. (1981). Proton-coupled electron transfer between $[Ru(bpy)_2(py)OH_2]^{2+}$ and $[Ru(bpy)_2(py)O]^{2+}$. A solvent isotope effect (k_{H2O}/k_{D2O}) of 16.1. *Journal of the American Chemical Society, 103*, 2897–2899. https://doi.org/10.1021/ja00400a083
98. Warren, J. J., Tronic, T. A., & Mayer, J. M. (2010). Thermochemistry of proton-coupled electron transfer reagents and its implications. *Chemical Reviews, 110*, 6961–7001. https://doi.org/10.1021/cr100085k
99. Huynh, M. H. V., & Meyer, T. J. (2007). Proton-coupled electron transfer. *Chemical Reviews, 107*, 5004–5064. https://doi.org/10.1021/cr0500030
100. Waluk, J. (2024). Nuclear quantum effects in proton or hydrogen transfer. *The Journal of Physical Chemistry Letters, 15*, 598–607. https://doi.org/10.1021/acs.jpclett.3c03368
101. Hammes-Schiffer, S., & Stuchebrukhov, A. A. (2010). Theory of coupled electron and proton transfer reactions. *Chemical Reviews, 110*, 6939–6960. https://doi.org/10.1021/cr1001436
102. Heisenberg, W. (1928). Zur theorie des derromagnetismus. *Zeitschrift für Physik, 49*, 619–636. https://doi.org/10.1007/BF01328601
103. Dirac, P. A. M. (1929). Quantum mechanics of many-electron systems. *Proceedings of the Royal Society of London, Series A, 123*, 714–733. https://doi.org/10.1098/rspa.1929.0094
104. Kotani, M. (1963). On the electronic state of iron in hemoglobins, with a short introduction to problems of quantum biophysis. *Reviews of Modern Physics, 35*, 717–720. https://doi.org/10.1103/RevModPhys.35.717
105. Matsen, F.A. (1964). Spin-free quantum chemistry. In P.-O. Löwdin (Eds.), *Advances in Quantum Chemistry* (Volume 1, pp.59–114). Elsevier. https://doi.org/10.1016/S0065-3276(08)60375-5.
106. Yamaguchi, K., Ohta, K., & Fueno, T. (1977). Localized natural orbitals of unstable molecules: Ozone. *Chemical Physics Letters, 50*, 266–270. https://doi.org/10.1016/0009-2614(77)80178-4
107. Yamaguchi, K., Tsunekawa, T., Toyoda, Y., & Fueno, T. (1988). Ab initio molecular orbital calculations of effective exchange integrals between transition metal ions. *Chemical Physics Letters, 143*, 371–376. https://doi.org/10.1016/0009-2614(88)87049-0
108. Lubitz, W., Chrysina, M., & Cox, N. (2019). Water oxidation in photosystem II. *Photosynthesis Research, 142*, 105–125. https://doi.org/10.1007/s11120-019-00648-3
109. Yano, J., & Yachandra, V. (2014). Mn_4Ca cluster in photosynthesis: Where and how water is oxidized to dioxygen. *Chemical Reviews, 114*, 4175–4205. https://doi.org/10.1021/cr4004874
110. Glöckner, C., Kern, J., Broser, M., Zouni, A., Yachandra, V., & Yano, J. J. (2013). Structural changes of the oxygen-evolving complex in photosystem II during the catalytic cycle. *Journal of Biological Chemistry, 288*, 22607–22620. https://doi.org/10.1074/jbc.M113.476622
111. Pantazis, D. A., Ames, W., Cox, N., Lubitz, W., & Neese, F. (2012). Two interconvertible structures that explain the spectroscopic properties of the oxygen-evolving complex of photosystem II in the S_2 state. *Angewandte Chemie International Edition, 51*, 9935–9940. https://doi.org/10.1002/anie.201204705
112. Guskov, A., Kern, J., Gabdulkhakov, A., Broser, M., Zouni, A., & Saenger, W. (2009). Cyanobacterial photosystem II at 2.9-Å resolution and the role of quinones, lipids, channels and chloride. *Nature Structural & Molecular Biology, 16*, 334–342. https://doi.org/10.1038/nsmb.1559
113. Shoji, M., Isobe, H., Shigeta, Y., Nakajima, T., & Yamaguchi, K. (2018). Concerted mechanism of water insertion and O_2 release during the S_4 to S_0 transition of the oxygen-evolving complex in photosystem II. *The Journal of Physical Chemistry B, 122*, 6491–6502. https://doi.org/10.1021/acs.jpcb.8b03465
114. Suga, M., Akita, F., Sugahara, M., Kubo, M., Nakajima, Y., Nakane, T., Yamashita, K., Umena, Y., Nakabayashi, M., Yamane, T., Nakano, T., Suzuki, M., Masuda, T., Inoue, S., Kimura, T., Nomura, T., Yonekura, S., Yu, L.-J., Sakamoto, T., … Shen, J.-R. (2017). Light-induced structural changes and the site of O=O bond formation in PSII caught by XFEL. *Nature, 543*, 131–135. https://doi.org/10.1038/nature21400
115. Shoji, M., Isobe, H., Miyagawa, K., & Yamaguchi, K. (2019). Possibility of the right-opened Mn-oxo intermediate (R-oxo(4444)) among all nine intermediates in the S_3 state of the oxygen-evolving complex of photosystem II revealed by large-scale QM/MM calculations. *Chemical Physics, 518*, 81–90. https://doi.org/10.1016/j.chemphys.2018.11.003
116. Ibrahim, M., Fransson, T., Chatterjee, R., Cheah, M. H., Hussein, R., Lassalle, L., Sutherlin, K. D., Young, I. D., Fuller, F. D., Gul, S., Kim, I.-S., Simon, P. S., de Lichtenberg, C., Chernev, P., Bogacz, I., Pham, C. C., Orville, A. M., Saichek, N., Northen, T., … Yano, J. (2020). Untangling the sequence of events during the $S_2 \rightarrow S_3$ transition in photosystem II and implications for the water oxidation mechanism. *Proceedings*

of the National Academy of Sciences, 117, 12624–12635. https://doi.org/10.1073/pnas.2000529117

117. Hussein, R., Ibrahim, M., Bhowmick, A., Simon, P. S., Chatterjee, R., Lassalle, L., Doyle, M., Bogacz, I., Kim, I.-S., Cheah, M. H., Gul, S., de Lichtenberg, C., Chernev, P., Pham, C. C., Young, I. D., Carbajo, S., Fuller, F. D., Alonso-Mori, R., Batyuk, A., … Yano, J. (2021). Structural dynamics in the water and proton channels of photosystem II during the S_2 to S_3 transition. *Nature Communications, 12*, 6531. https://doi.org/10.1038/s41467-021-26781-z
118. Bhowmick, A., Hussein, R., Bogacz, I., Simon, P.S., Ibrahim, M., Chatterjee, R., Doyle, M.D., Cheah, M.H., Fransson, T., Chernev, P., Kim, I.S., Makita, H., Dasgupta, M., Kaminsky, C.J., Zhang, M., Gätcke, J., Haupt, S., Nangca, I.I., Keable, S.M., Aydin, A.O., Tono, K., Owada, S., Gee, L.B., Fuller, F.D., Batyuk, A., Alonso-Mori, R., Holton, J.M., Paley, D.W., Moriarty, N.W., Mamedov, F., Adams, P.D., Brewster, A.S., Dobbek, H., Sauter, N.K., Bergmann, U., Zouni, A., Messinger, J., Kern, J., Yano, J., & Yachandra, V.K. (2023). Structural evidence for intermediates during O_2 formation in photosystem II. *Nature*, 617, 629–636 (2023). https://doi.org/10.1038/s41586-023-06038-z
119. Li, H., Nakajima, Y., Nango, E., Owada, S., Yamada, D., Hashimoto, K., Luo, F., Tanaka, R., Akita, F., Kato, K., Kang, J., Saitoh, Y., Kishi, S., Yu, H., Matsubara, N., Fujii, H., Sugahara, M., Suzuki, M., Masuda, T., … Shen, J.-R. (2024). Oxygen-evolving photosystem II structures during S_1–S_2–S_3 transitions. *Nature, 626*, 670–677. https://doi.org/10.1038/s41586-023-06987-5
120. Wikstrom, M. K. F. (1977). Proton pump coupled to cytochrome *c* oxidase in mitochondria. *Nature, 266*, 271–273. https://doi.org/10.1038/266271a0
121. Ogura, T., Takahashi, S., Hirota, S., Shinzawa-Itoh, K., Yoshikawa, S., Appleman, E. H., & Kitagawa, T. (1993). Time-resolved resonance Raman elucidation of the pathway for dioxygen reduction by cytochrome c oxidase. *Journal of the American Chemical Society, 115*, 8527–8536. https://doi.org/10.1021/ja00072a002
122. Proshlyakov, D. A., Ogura, T., Shinzawa-Itoh, K., Yoshikawa, S., Appleman, E. H., & Kitagawa, T. (1994). Selective resonance Raman observation of the "607 nm" form generated in the reaction of oxidized cytochrome *c* oxidase with hydrogen peroxide. *Journal of Biological Chemistry, 269*, 29385–29388. https://doi.org/10.1016/S0021-9258(18)43890-2
123. Iwata, S., Ostermeier, C., Ludwig, B., & Michel, H. (1995). Structure at 2.8 Å resolution of cytochrome *c* oxidase from *Paracoccus denitrificans*. *Nature, 376*, 660–669. https://doi.org/10.1038/376660a0
124. Ferguson-Miller, S., & Babcock, G. T. (1996). Heme/copper terminal oxidases. *Chemical Reviews, 96*, 2889–2908. https://doi.org/10.1021/cr950051s
125. Michel, H., Behr, J., Harrenga, A., & Kannt, A. (1998). Cytochrome *c* oxidase: Structure and spectroscopy. *Annual Review of Biophysics, 27*, 329–356. https://doi.org/10.1146/annurev.biophys.27.1.329
126. Proshlyakov, D. A., Pressler, M. A., & Babcock, G. T. (1998). Dioxygen activation and bond cleavage by mixed-valence cytochrome c oxidase. *Proceedings of the National Academy of Sciences, 95*, 8020–8025. https://doi.org/10.1073/pnas.95.14.8020
127. Yoshioka, Y., Kubo, S., Yamaguchi, K., & Saito, I. (1998). An ab initio molecular orbital study of a binuclear dioxygen complex as a model of the binuclear active site in cytochrome *c* oxidase. *Chemical Physics Letters, 294*, 459–467. https://doi.org/10.1016/S0009-2614(98)00924-5
128. Blomberg, M. R. A., Siegbahn, P. E. M., & Babcock, G. T. (1998). Modeling electron transfer in biochemistry: A quantum chemical study of charge separation in *Rhodobacter sphaeroides* and photosystem II. *Journal of the American Chemical Society, 120*, 8812–8824. https://doi.org/10.1021/ja9805268
129. Yoshioka, Y., Kawai, H., & Yamaguchi, K. (2003). Theoretical study of role of H_2O molecule on initial stage of reduction of O_2 molecule in active site of cytochrome *c* oxidase. *Chemical Physics Letters, 374*, 45–52. https://doi.org/10.1016/S0009-2614(03)00683-3
130. Brzezinski, P., & Gennis, R. B. (2008). Cytochrome *c* oxidase: Exciting progress and remaining mysteries. *Journal of Bioenergetics and Biomembranes, 40*, 521–531. https://doi.org/10.1007/s10863-008-9181-7
131. Noodleman, L., Du, W.-G.H., McRee, D., Chen, Y., Goh, T., & Götz, A. W. (2020). Coupled transport of electrons and protons in a bacterial cytochrome *c* oxidase—DFT calculated properties compared to structures and spectroscopies. *Physical Chemistry Chemical Physics, 22*, 26652–26668. https://doi.org/10.1039/D0CP04848H
132. Jose, A., Schaefer, A. W., Roveda, A. C., Jr., Transue, W. J., Choi, S. K., Ding, Z., Gennis, R. B., & Solomon, E. I. (2021). The three-spin intermediate at the O-O cleavage and proton-pumping junction in heme–Cu oxidases. *Science, 373*, 1225–1229. https://doi.org/10.1126/science.abh3209
133. Blomberg, M. R. A. (2021). The redox-active tyrosine is essential for proton pumping in cytochrome c oxidase. *Frontiers in Chemistry, 9*, 640155. https://doi.org/10.3389/fchem.2021.640155
134. Wikström, M., Gennis, R. B., & Rich, P. R. (2023). Structures of the intermediates in the catalytic cycle of mitochondrial cytochrome *c* oxidase. *Biochimica et Biophysica Acta - Bioenergetics, 1864*, 148933. https://doi.org/10.1016/j.bbabio.2022.148933
135. Ishigami, I., Sierra, R. G., Su, Z., Peck, A., Wang, C., Poitevin, F., Lisova, S., Hayes, B., Moss, F. R., III., Boutet, S., Sublett, R. E., Yoon, C. H., Yeh, S.-R., & Rousseau, D. L. (2023). Structural insights into functional properties of the oxidized form of cytochrome *c* oxidase. *Nature Communications, 14*, 5752. https://doi.org/10.1038/s41467-023-41533-x
136. Shimada, A., Tsukihara, T., & Yoshikawa, S. (2023). Recent progress in experimental studies on the catalytic mechanism of cytochrome *c* oxidase. *Frontiers in Chemistry, 11*, 1108190. https://doi.org/10.3389/fchem.2023.1108190
137. Wada, T., Tsuge, K., & Tanaka, K. (2000). Electrochemical oxidation of water to dioxygen catalyzed by the oxidized form of the bis(ruthenium – hydroxo) complex in H_2O. *Angewandte Chemie International Edition, 39*, 1479–1482. https://doi.org/10.1002/(SICI)1521-3773(20000417)39:8%3c1479::AID-ANIE1479%3e3.0.CO;2-4
138. Tanaka, K., Isobe, H., Yamanaka, S., & Yamaguchi, K. (2012). Similarities of artificial photosystems by ruthenium oxo complexes and native water splitting systems. *Proceedings of the National Academy of Sciences, 109*, 15600–15605. https://doi.org/10.1073/pnas.1120705109
139. Isobe, H., Tanaka, K., Shen, J.-R., & Yamaguchi, K. (2014). Water oxidation chemistry of a synthetic dinuclear ruthenium complex containing redox-active quinone ligands. *Inorganic Chemistry, 53*, 3973–3984. https://doi.org/10.1021/ic402340d

140. Kumagai, Y., Takabe, R., Nakazono, T., Shoji, M., Isobe, H., Yamaguchi, K., Misawa-Suzuki, T., Nagao, H., & Wada, T. (2024). Water oxidation utilizing a ruthenium complex featuring a phenolic moiety inspired by the oxygen-evolving centre (OEC) of photosystem II. *Sustainable Energy & Fuels, 8*, 905–913. https://doi.org/10.1039/D3SE01610B
141. Meyer, T. J., Huynh, M. H. V., & Thorp, H. H. (2007). The possible role of proton-coupled electron transfer (PCET) in water oxidation by photosystem II. *Angewandte Chemie International Edition, 46*, 5284–5304. https://doi.org/10.1002/anie.200600917
142. Shoji, M., Isobe, H., Shigeta, Y., Nakajima, T., & Yamaguchi, K. (2018). Nonadiabatic one-electron transfer mechanism for the O-O bond formation in the oxygen-evolving complex of photosystem II. *Chemical Physics Letters, 698*, 138–146. https://doi.org/10.1016/j.cplett.2018.02.056
143. Vogiatzis, K. D., Polynski, M. V., Kirkland, J. K., Townsend, J., Hashemi, A., Liu, C., & Pidko, E. A. (2019). Computational approach to molecular catalysis by 3d transition metals: Challenges and opportunities. *Chemical Reviews, 119*, 2453–2523. https://doi.org/10.1021/acs.chemrev.8b00361
144. Yamaguchi, K., Yamanaka, S., Shoji, M., Isobe, H., Kawakami, T., Yamada, S., & Okumura, M. M. (2014). Theory of chemical bonds in metalloenzymes XIX: Labile manganese oxygen bonds of the $CaMn_4O_5$ cluster in oxygen evolving complex of photosystem II. *Molecular Physics, 112*, 485–507. https://doi.org/10.1080/00268976.2013.842009
145. Hunter, B. M., Gray, H. B., & Müller, A. M. (2016). Earth-abundant heterogeneous water oxidation catalysts. *Chemical Reviews, 116*, 14120–14136. https://doi.org/10.1021/acs.chemrev.6b00398

Authors and Affiliations

Kizashi Yamaguchi[1,2,3] · Koichi Miyagawa[2] · Mitsuo Shoji[4] · Hiroshi Isobe[5] · Takashi Kawakami[3,6]

✉ Kizashi Yamaguchi
yama@chem.sci.osaka-u.ac.jp

✉ Koichi Miyagawa
miyagawak@sanken.osaka-u.ac.jp

✉ Takashi Kawakami
kawakami@chem.sci.osaka-u.ac.jp

[1] Center for Quantum Information and Quantum Biology, Osaka University, Toyonaka, Osaka 560-0043, Japan

[2] SANKEN, Osaka University, Ibaraki, Osaka 567-0047, Japan

[3] RIKEN Center for Computational Science, Kobe, Hyogo 650-0047, Japan

[4] Present Address: Center of Computational Sciences, University of Tsukuba, Tsukuba, Ibaraki 305-8577, Japan

[5] Graduate School of Natural Science and Technology, Research Institute for Interdisciplinary Science, Okayama University, Okayama 700-8530, Japan

[6] Graduate School of Science, Osaka University, Toyonaka, Osaka 560-0043, Japan